

Article

Spectral Structure and Many-Body Dynamics of Ultracold Bosons in a Double-Well

Frank Schäfer^{1,2,*} , Miguel A. Bastarrachea-Magnani^{1,3} , Axel U. J. Lode¹ ,
Laurent de Forges de Parny^{1,4} and Andreas Buchleitner^{1,5,*}

¹ Physikalisches Institut, Albert-Ludwigs-Universität Freiburg, Hermann-Herder-Straße 3, D-79104 Freiburg, Germany; mbastarrachea@phys.au.dk (M.A.B.-M.); auj.lode@gmail.com (A.U.J.L.); laurentdeforgesdeparny@gmail.com (L.d.F.d.P.)

² Department of Physics, University of Basel, Klingelbergstrasse 82, CH-4056 Basel, Switzerland

³ Department of Physics and Astronomy, Aarhus University, Ny Munkegade, DK-8000 Aarhus C, Denmark

⁴ ACRI-ST, 260 route du Pin Montard, 06904 Sophia Antipolis CEDEX, France

⁵ Freiburg Institute for Advanced Studies (FRIAS), Albert-Ludwigs-Universität Freiburg, Albertstr. 19, D-79104 Freiburg, Germany

* Correspondence: frank.schaefer@unibas.ch (F.S.); a.buchleitner@physik.uni-freiburg.de (A.B.)

Received: 11 February 2020; Accepted: 20 March 2020; Published: 26 March 2020



Abstract: We examine the spectral structure and many-body dynamics of two and three repulsively interacting bosons trapped in a one-dimensional double-well, for variable barrier height, inter-particle interaction strength, and initial conditions. By exact diagonalization of the many-particle Hamiltonian, we specifically explore the dynamical behavior of the particles launched either at the single-particle ground state or saddle-point energy, in a time-independent potential. We complement these results by a characterization of the cross-over from diabatic to quasi-adiabatic evolution under finite-time switching of the potential barrier, via the associated time evolution of a single particle's von Neumann entropy. This is achieved with the help of the multiconfigurational time-dependent Hartree method for indistinguishable particles (MCTDH-X)—which also allows us to extrapolate our results for increasing particle numbers.

Keywords: Bosonic systems; ultracold atomic gases; tunneling and Josephson effect; Bose–Einstein condensates in periodic potentials

1. Introduction

The detailed microscopic understanding of interacting many-particle quantum dynamics in state-of-the-art experiments with ultracold atoms [1–10] in well-characterized potential landscapes remains a challenging task for theory: While a large arsenal of advanced numerical techniques has been developed over the past two decades to efficiently simulate interacting many-particle dynamics [11–15], all of them must ultimately surrender when confronted with truly complex dynamics, i.e., under conditions where a generic initial state fully explores, on sufficiently long time scales, an exponentially large Hilbert space in the number of particles and/or degrees of freedom. By the very meaning of complexity, even the most efficient numerical methods can only be expected to yield reliable results when the dynamics can be restricted to finite sub-spaces of the exponentially large Hilbert spaces—either by reducing the time window over which the evolution is followed, or by choosing physical situations which a priori confine the many-particle state. This has been long understood in the light–matter interaction of atoms and molecules [16], as well as in quantum chaos [17], and meets revived interest given the experimental progress in the control of cold matter [18].

While it is, therefore, clear that the only promising route for an efficient characterization of large and complex quantum systems can be through effective descriptions—such as offered,

e.g., by the theory of open quantum systems [19–22], modern semiclassics [23], or random matrix theory [24,25]—there is an intermediate range of system sizes where efficient numerical methods can (a) be gauged against each other, to benchmark their quantitative reliability, without any a priori restriction on the explored portion of Hilbert space, and (b) contribute to gauge effective theories against (numerically) exact solutions [26–28], at spectral densities where quantum granular effects induce possibly sizeable deviations [29] from effective theory predictions (which always rely on some level of coarse graining). In our view, it is this intermediate system sizes where efficient methods of numerical simulation develop their full potential, since they can inspire and ease the development, e.g., of powerful statistical methods and paradigms (such as scaling properties [18,26,30])—which then enable robust predictions in the realm of fully unfolding complexity.

In the present paper, we contribute to this line of research by exploring the spectral and dynamical properties of a few bosonic particles loaded into a symmetric double-well potential, with static or switchable barrier. *Prima facie*, this is a well-known and text-book-like example, yet with a panoply of experimental realizations, and of paradigmatic relevance as an incarnation of Josephson dynamics [4,31–47] or as the elementary building block of quantum dynamics in lattice-like structures [48], and quickly defines a formidable numerical challenge if only one admits excitations far beyond the immediate vicinity of the ground state energy, and seeks to accurately monitor the long-term dynamics of two or more particles. We will see how the spectral structure of the single-particle problem is amended by adding a second, identical particle, and how finite-strength interactions restructure the many-particle spectrum and eigenstates, throughout the excitation spectrum up to the vicinity of the potential barrier.

Ultimately, we have two main goals: First, we want to shed light onto the nature of the tunneling processes of two, repulsively interacting bosons launched either at the ground state or saddle-point energy. Secondly, we want to study the transition between diabatic and adiabatic switching of the potential barrier for different particle numbers. Importantly, we will find that tunneling is described by a second-order two-particle process and not by a direct first-order two-particle process. We underpin our studies by information from the respective regimes in the spectrum. These scenarios come with very different challenges for the numerical treatment, because the evaluation of the time evolution generated by a time-independent ordinary differential equation in case of a static potential significantly differs from the one described by a time-dependent ordinary differential equation in case of a switchable barrier. To achieve our above two main goals and as a central aspect of our present contribution, we employ a variety of different numerical approaches which, by accounting for the complete spectral structure of the double-well (rather than the lowest-lying band alone), go far beyond widely used single-band Bose–Hubbard models.

Here and in the following, we use the term “many-body/particle”, albeit the systems we consider are composed of a relatively small number of particles. Please note that our considerations are from first principles and start from the many-body Hamiltonian. Moreover, it has been shown theoretically [17,49,50] and experimentally [1,2] that the physics of interacting few-body systems can very quickly approach the many-body limit.

The spectral information thus generated allows us to decipher characteristic features of the many-particle dynamics, for distinct choices of the initial condition, and over a wide range of interaction strengths, for static as well as for diabatically or (quasi-)adiabatically ramped potential barriers. Finally, we illustrate, through an analysis of the von Neumann entropy of the (reduced) single-particle density matrix, how such transition from diabatic to (quasi-) adiabatic switching controls the effectively explored sub-volume of Hilbert space, and how robust coarse grained features of the resulting “phase diagram” emerge as the particle number is increased from two to ten. The latter case can only be treated with the help of the MCTDH-X [28,51,52] method which has been verified against exact [27,28] and experimental [53] results and is reviewed in Ref. [15]. Here, we push MCTDH-X to its limits in monitoring long-term dynamics of rather moderate, mesoscopic particle numbers, in the presence of strong, switching-induced excitations (“quenches”).

The paper is organized as follows: The theoretical framework, including a brief description of the numerical methods, is presented in Section 2. Section 3 is devoted to the discussion of the spectral and eigenstate structure of the problem at hand. First, Section 3.1 discusses how the energy spectrum depends on both the tunneling barrier height and the inter-particle interaction strength, for two and three particles. Next, in Section 3.2, we study few-body correlations encoded in the few-body eigenstates. This prepares our analysis of the dynamics in Section 4. In Section 4.1, we investigate the dynamics of two particles in a static double-well potential, initially prepared in two different states: A superposition of low-lying states, and a superposition of excited states with energies close to the saddle point. Finally, we consider the scenario of a time-dependent potential in Section 4.2: With the atoms initially prepared in the ground state of a harmonic trap, a central barrier is ramped up, and the thereby induced dynamics can be tuned from diabatic to (quasi-) adiabatic by appropriate control of the ramping time. Our results are summarized in Section 5.

2. Hamiltonian and Methods

2.1. Hamiltonian of Trapped Interacting Bosons

The Hamiltonian of N spinless, ultracold atoms with repulsive contact interaction and confined to a one-dimensional double-well potential reads in atomic units

$$H = \sum_i^N \left(-\frac{1}{2} \frac{d^2}{dx_i^2} + V(x_i, t) \right) + \frac{\lambda}{2} \sum_{i \neq j} \delta(x_i - x_j), \quad (1)$$

where

$$V(x_i, t) = \frac{x_i^2}{2} + A(t)e^{-x_i^2/2} \quad (2)$$

allows for a non-trivial time dependence of the potential barrier, through the time dependence of $A(t)$, x_i denotes the position of the i th particle, and the repulsive interaction strength $\lambda > 0$ is determined by the s-wave scattering length and the transverse confinement [54].

The minimum of $V(x_i, t)$ is located at $x = 0$ if $A(t) < 1$ (single-well), or at $x = \pm \sqrt{2 \ln(A(t))}$ if $A(t) \geq 1$ (double-well). Both static and time-dependent barriers will be considered. In the static case, the central barrier amplitude is constant, $A(t) = A_{\max}$, whereas in the time-dependent scenario, the amplitude is ramped up linearly according to

$$A(t) = A_{\max} \times \begin{cases} t/T_{\text{ramp}}, & t < T_{\text{ramp}}, \\ 1, & t \geq T_{\text{ramp}}. \end{cases} \quad (3)$$

2.2. Numerical Methods and Observables

The spectral and dynamical properties of the Hamiltonian (1) are numerically investigated by using three approaches: the Fourier Grid Hamiltonian (FGH), the Bose–Hubbard (BH) representation of a continuous potential, and the multiconfigurational time-dependent Hartree method for indistinguishable particles (MCTDH-X); see Appendices A, B and C, respectively.

Each of these is suited for a specific task. We use FGH and BH which, ultimately, rely on different basis set representations of the Hamiltonian, to infer the spectrum of $N \leq 2$ and $N = 3$ interacting bosons, by direct diagonalization. FGH is also useful for the investigation of the quenched dynamics when a harmonic potential with $A_{\max} = 0$ at $t = 0$ is suddenly transformed into a static double-well with fixed barrier $A_{\max} = \text{const.}$ at $t > 0$ (in other words, $T_{\text{ramp}} \rightarrow 0$ in Equation (3)). For our study of the case of $N \leq 10$ interacting bosons in a time-dependent double-well with $T_{\text{ramp}} \neq 0$, we use the MCTDH-X method which enables accurate results for the dynamics, but cannot provide the complete

spectral information as the BH/FGH methods. Since dynamical properties of interacting many-particle systems emerge, already at rather small particle numbers [17], the combination of all three approaches can be considered complementary.

FGH and BH yield the N -particle eigenenergies

$$H|\Psi_n\rangle = E_n^{NP}(A_{\max}, \lambda)|\Psi_n\rangle, \tag{4}$$

with $|\Psi_n\rangle$ the N -particle eigenvector with quantum number n . All eigenstates are normalized to unity, throughout this paper. The quantity

$$|\psi_n(x_1, x_2, \dots, x_N)|^2 = |\langle x_1, \dots, x_N | \Psi_n \rangle|^2 \tag{5}$$

yields the associated probability density to find N bosons located at positions x_1, x_2, \dots, x_N , respectively. Visualizations thereof reflect the correlations between the positions of the particles [37,38,40,41,43,44,53,55,56], which can be assessed, e.g., through their entanglement. A possible (though certainly non-exhaustive) quantifier of the non-separability of a general many-particle state $|\Psi(t)\rangle$ is given by the von Neumann entropy

$$S(t) = -\text{Tr} [\rho^{1P}(t) \ln \rho^{1P}(t)] \tag{6}$$

of the reduced single-particle density matrix [37,38,57–59], where $\rho^{1P}(x, x', t)$ is defined as the trace over all degrees of freedom of all but one boson of the full density operator, i.e.,

$$\rho^{1P}(t) = \text{Tr}_{2,\dots,N} [|\Psi(t)\rangle\langle\Psi(t)|] . \tag{7}$$

In particular, $S = 0$ if the state is *separable*, while large values of S are a hallmark of a strongly *entangled* many-particle state [60–64]. We note that wide-spread mean-field approaches like the time-dependent Gross–Pitaevskii equation presuppose a separable many-body state with $S = 0$; any $S \neq 0$ thus heralds the breakdown of such a mean-field description.

To characterize the dynamics of two bosons, we monitor the time evolution of the particles' probabilities to reside both in the right (RR) or left (LL) well, or of each occupying one well (LR), given by [55]

$$\begin{aligned} P_{(LL)}(t) &= \int_{x_{\min}}^0 dx_1 \int_{x_{\min}}^0 dx_2 |\psi(x_1, x_2; t)|^2, \\ P_{(RR)}(t) &= \int_0^{x_{\max}} dx_1 \int_0^{x_{\max}} dx_2 |\psi(x_1, x_2; t)|^2, \\ P_{(LR)}(t) &= 2 \cdot \int_{x_{\min}}^0 dx_1 \int_0^{x_{\max}} dx_2 |\psi(x_1, x_2; t)|^2, \end{aligned} \tag{8}$$

where we defined the three mutually distinct domains $(LL) = (x_1 < 0, x_2 < 0)$, $(RR) = (x_1 \geq 0, x_2 \geq 0)$, and $(LR) = (x_1 < 0, x_2 \geq 0) \vee (x_1 \geq 0, x_2 < 0)$. We also introduced the minimum (x_{\min}) and maximum (x_{\max}) values of the grid in configuration space employed in the numerical approaches. In addition, we evaluate the time-integrated probability current

$$J_{(RR \rightarrow LR)}(t) = 2 \cdot \int_0^t dt' \int_0^{x_{\max}} dx_2 \text{Im} \left[\psi^*(x_1, x_2; t') \frac{\partial}{\partial x_1} \psi(x_1, x_2; t') \right]_{x_1=0}, \tag{9}$$

where the factor 2 accounts for the bosonic symmetry. $J_{(RR \rightarrow LR)}$ is derived [65] from the continuity equation and measures the probability flux within a time interval t from domain (RR) to domain (LR). This quantity is particularly important to distinguish first-order pairwise tunneling ($RR \rightarrow LL$) from second-order pairwise tunneling ($RR \rightarrow LR \rightarrow LL$). First-order pairwise tunneling was observed [65],

e.g., for attractively interacting bosons in a double-well, where $J_{(RR \rightarrow LR)}(t) = 0, \forall t$, when the particles are initially prepared in one well.

3. Structure of Spectrum and Eigenstates

3.1. Few-Body Excitation Spectra

Since the dynamics of the system is ultimately encoded in its spectrum, we first discuss the parametric evolution of the eigenvalues (4) of $N = 1, 2$ and 3 bosons with both the central barrier height A_{\max} and the interaction strength λ .

The single-particle spectrum is obtained by solving the time-independent Schrödinger equation

$$\left(-\frac{1}{2} \frac{d^2}{dx^2} + \frac{x^2}{2} + A_{\max} e^{-x^2/2} \right) \psi_n(x) = E_n^{1P} \psi_n(x). \tag{10}$$

Figure 1 shows the evolution of the single-particle eigenenergies E_n^{1P} as the central barrier height A_{\max} is continuously increased from a harmonic trap ($A_{\max} = 0$) to a deep double-well ($A_{\max} = 30$).

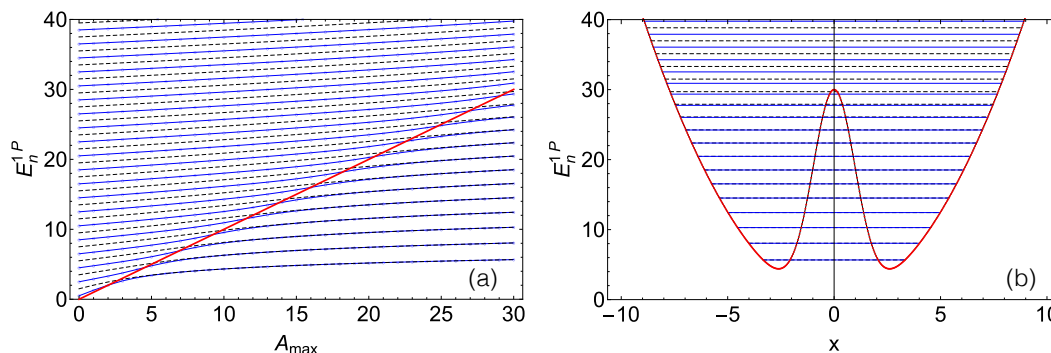


Figure 1. Single-particle eigenenergies E_n^{1P} of Equation (10), (a) as a function of the tunneling barrier height A_{\max} , and (b) for $A_{\max} = 30$ in the double-well potential (red). The red line in (a) indicates the central barrier’s height on the energy axis. Even- (blue lines) and odd-parity (black dashed) states become nearly degenerate as A_{\max} is increased. Employed parameter values for the FGH method (see Appendix A): $x_{\max} = -x_{\min} = 40$, $N_{\text{cut}} = 330$, and $N_{\text{Grid}} = 2047$.

In the harmonic limit, the spectrum exhibits the well-known harmonic oscillator structure $E_n^{1P}(A_{\max} = 0) = n + 1/2$. As the eigenenergies dive into the region below the barrier A_{\max} (indicated by the red diagonal in Figure 1a), the odd and even harmonic oscillator states become (nearly) degenerate. Sufficiently above A_{\max} , the energies are only weakly perturbed by the central barrier and we essentially recover the harmonic oscillator energy levels. In the limit $A_{\max} \rightarrow \infty$, the two wells decouple, leading to a fully degenerate harmonic oscillator spectrum.

From the structure of the single-particle spectrum, we can already anticipate that different dynamical behaviors can be expected for initial conditions with energies chosen below or above A_{\max} , as will be elaborated upon, subsequently.

We now turn our attention to the spectrum of two particles obtained with the FGH method. The exact two-body spectrum is calculated by diagonalization of Equation (1) represented in the single-particle basis, as explained in Appendix A. Figure 2a shows that for $A_{\max} = 0$, we recover the well-known spectrum of two non-interacting bosons in a harmonic trap, i.e., $E_n^{2P}(A_{\max} = 0) = n + 1$, with $n = n_1 + n_2$ and degeneracy $g = n/2 + 1$ ($g = (n + 1)/2$) for even (odd) $n \geq 0$. Here again, raising the central barrier gradually introduces a further degeneracy in the spectrum: The first three lowest-lying states become (nearly) degenerate when increasing A_{\max} . This effect, also discussed in

Ref. [38], is a direct consequence of the two-fold degeneracy of the single-particle ground state of the double-well, since all the eigenstates $|\Psi_0\Psi_0\rangle$, $|\Psi_0\Psi_1\rangle$ and $|\Psi_1\Psi_1\rangle$, with

$$|\Psi_n\Psi_m\rangle \equiv \frac{|\Psi_n\rangle \otimes |\Psi_m\rangle + |\Psi_m\rangle \otimes |\Psi_n\rangle}{\sqrt{2}\sqrt{1 + \langle \Psi_n | \Psi_m \rangle}}, \tag{11}$$

acquire the same energy value at large A_{\max} (see Equations (A9) and (A10)). For higher excitations, an analogous effect is observed: e.g., the energies of the states $|\Psi_2\Psi_0\rangle$, $|\Psi_2\Psi_1\rangle$, $|\Psi_3\Psi_0\rangle$ and $|\Psi_3\Psi_1\rangle$, respectively given by the sums of single-particle energies, $E_2^{1P} + E_0^{1P}$, $E_2^{1P} + E_1^{1P}$, $E_3^{1P} + E_0^{1P}$, and $E_3^{1P} + E_1^{1P}$, converge when increasing A_{\max} , since $E_1^{1P} \simeq E_0^{1P}$ and $E_3^{1P} \simeq E_2^{1P}$. Therefore, the entire spectrum of two non-interacting bosons, plotted in Figure 2a, can be understood solely in terms of the single-particle spectrum. The emergence of the sequence of quasi-degenerate states is clearly observed below the separatrix $E^{2P} = 2A_{\max}$, plotted in red in Figure 2a.

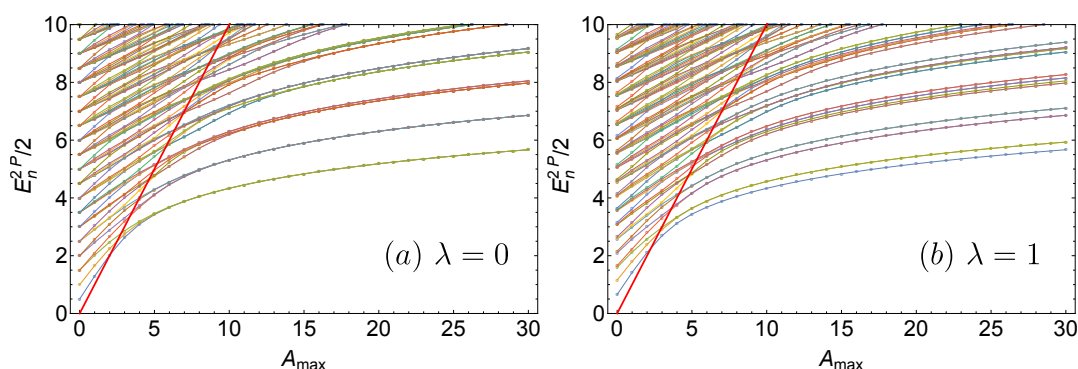


Figure 2. Two-particle eigenenergies E_n^{2P} per particle, Equation (4), as a function of the (static) tunneling barrier height A_{\max} , for interaction strengths (a) $\lambda = 0$ and (b) $\lambda = 1$. Finite interactions partially or totally lift the degeneracy of the eigenenergies, depending on the considered quantum number. The red line indicates the effective potential barrier height—which is twice the barrier height for a single particle, i.e., $2A_{\max}$. Parameter values for the FGH method: $x_{\max} = -x_{\min} = 40$, $N_{\text{cut}} = 330$, and $N_{\text{Grid}} = 2047$.

Turning on the interaction changes the structure of the energy spectrum, as shown in Figure 2b. The calculation of the energy spectrum in the general case $A_{\max} \neq 0$ requires a numerical treatment, whereas an analytical solution exists for the harmonic trap with $A_{\max} = 0$ and $N = 2$ [59,66]. The most striking feature is the opening of an energy gap, clearly observed at large A_{\max} : At the ground-state level, the three-fold degenerate states for $\lambda = 0$ split into a unique ground state which remains unperturbed by the interaction, plus two (nearly) degenerate excited states which are affected by the non-vanishing interaction strength $\lambda \neq 0$. This behavior was already discussed in Ref. [38] for a polynomial double-well. Our present results show that this effect is also observed in the excitation spectrum below the separatrix $2A_{\max}$. For instance, the first excited state manifold of the $\lambda = 0$ limit (see Figure 2a, in the range $A_{\max} \geq 10$), which is four-fold degenerate, splits (for $\lambda = 1$, Figure 2b) into two (nearly) degenerate states unperturbed by the interaction, plus two (nearly) degenerate states slightly shifted by the interaction. The presence of these energy gaps in the spectrum will be essential for our understanding of the many-particle dynamics discussed in the next sections.

Consideration of a deep double-well, e.g., $A_{\max} = 30$, allows for a better understanding of interaction-induced spectral features, as shown in Figure 3.

Indeed, for energies $E_n^{2P} \ll 2A_{\max}$, one can approximate the two wells by two decoupled harmonic traps with vanishing tunneling coupling. Flat energy levels correspond to the situation where the particles are almost completely localized in opposite wells and, consequently, do not interact. The remaining energy levels represent configurations where both particles occupy the same well. The spectral lines then approach the next higher-lying manifold at strong interaction, e.g., $\lambda \simeq 10$.

In the limit of $\lambda \rightarrow \infty$, one recovers the Tonks-Girardeau (or fermionization) limit where these states become degenerate [38,43,44] with the second excited state manifold. Please note that by construction, this limit is out of reach for the single-band (or two-mode) approximation widely used in the literature. Figure 3 shows that the trend towards degeneracy between even and odd states with increasing λ (fermionization process) is not restricted to the first spectral manifolds, but clearly manifests itself in the entire spectral range $E_n^{2P} \ll 2A_{\max}$.

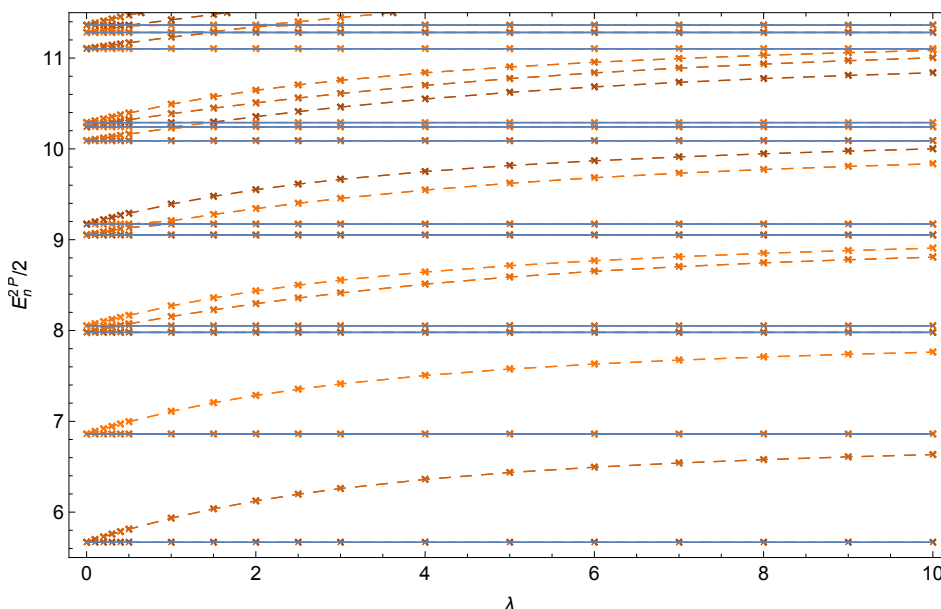


Figure 3. Two-particle eigenenergies E_n^{2P} per particle, Equation (4), as a function of the inter-particle interaction strength λ , in a deep double-well with $A_{\max} = 30$. Flat energies (continuous lines) correspond to the situation where the particles are almost completely localized in opposite wells and do not interact. Increasing λ tends to induce a degeneracy between even and odd states (fermionization process). FGH parameters: $x_{\max} = -x_{\min} = 40$, $N_{\text{cut}} = 330$, and $N_{\text{Grid}} = 2047$.

The situation is (again) very different for three interacting particles [42]: Figure 4 shows the three-particle energy levels, for $A_{\max} = 30$, as a function of the interaction strength U . All states are sensitive to the interaction and we observe two manifolds of states—states which exhibit interactions of two particles (full lines), and states which exhibit interactions of three particles (dashed lines). In contrast to the two-particle case, the ground state remains two-fold quasi-degenerate at large λ . Please note that the present three-particle results were obtained with the BH method (see Appendix B), since the Hamiltonian matrix is sparse in the BH representation, and therefore allows for computationally more efficient handling than the FGH method, for which the eigenenergies converge only slowly as a function of N_{cut} [56]. Furthermore, in the BH method $U \equiv \lambda \sum_i |w_{0i}|^4$, cf. Equation (A21), substitutes for λ used in the FGH calculations.

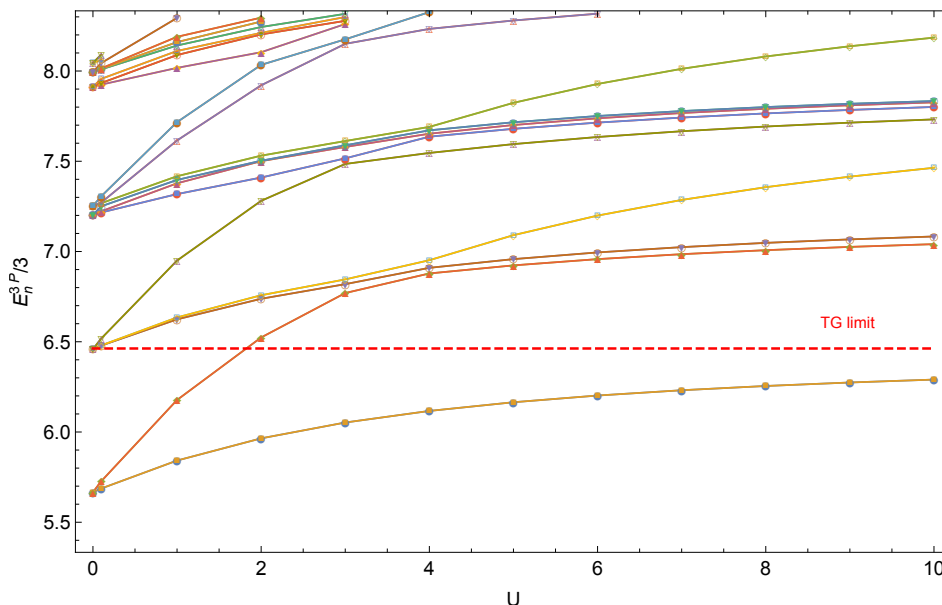


Figure 4. Three-particle eigenenergies E_n^{3P} per particle, Equation (4), as a function of the inter-particle interaction strength $U \equiv \lambda \sum_i |w_{0i}|^4$ (see Appendix B), with $A_{\max} = 30$. Dashed (continuous) lines represent eigenstates with three (two) particles on the same well, and the red horizontal line indicates the Tonks-Girardeau (TG) limit for the ground state. Parameters employed for the BH method (see App. B): $x_{\max} = -x_{\min} = 10$, and $L = 231$.

3.2. Eigenstate Structure and Few-Body Correlations

Let us now inspect the associated many-particle eigenstates and the spatial correlations encoded into them, again as a function of both the central barrier height A_{\max} and the interaction strength λ . The probability density, Equation (5), provides useful intuition. For two non-interacting bosons, the probability densities $|\psi_n(x_1, x_2)|^2$ are plotted in Figure 5, for energetically low- and high-lying eigenstates, as well as for different choices of the barrier height A_{\max} .

At low energies ($n = 0, 1, 2$), and with increasing barrier height $A_{\max} \rightarrow \infty$, $|\psi_n(x_1 = 0, x_2)|^2 \rightarrow 0$ and $|\psi_n(x_1, x_2 = 0)|^2 \rightarrow 0$. Consequently, the maxima of the probability density symmetrically split into the two or four corners of configuration space [37,38,67]. For $n = 1$, the nodal line $x_1 = -x_2$ originates from the superposition of even and odd (nearly) degenerate single-particle states. Please note that the associated eigenenergies are quasi-degenerate at $A_{\max} = 30$: $E_{n=0,1,2}^{2P} \simeq 11.34$. At higher excitations, where the spectrum must progressively approach that of a harmonic oscillator (recall Figure 1b), the eigenstates exhibit a metamorphosis, sometimes even displaying a maximum at the saddle point, see, e.g., $n = 76$, $A_{\max} = 10$, and thus reminiscent of barrier states of the single-particle problem.

Interactions affect the spatial correlations in many ways, as shown in Figure 6 for $\lambda = 1$: Comparison to Figure 5 shows that for $n = 0 - 3$, the interaction slightly stretches the maxima of the eigenstates along the anti-diagonal $x_2 = -x_1$ [38], and in some cases suppresses the amplitudes for double-occupancy of either site or that of delocalization over both sites. In a deep double-well, e.g., $A_{\max} = 30$, the three-fold (nearly) degenerate non-interacting eigenstates $n = 0 - 2$ of Figure 5 split into a unique ground state and two (nearly) degenerate eigenstates $n = 1, 2$. At higher excitations ($n = 76$), we observe product states in the relative $\propto x_1 - x_2$ and center-of-mass $\propto x_1 + x_2$ coordinates (see Figure 6 for $A_{\max} = 0$), and, therefore, also for these states correlated tunneling is expected, as opposed to the independent tunneling imprinted into the eigenstates in Figure 5. The impact of interactions on states in the vicinity of the separatrix is mainly highlighted by a suppression of the density maximum around $x_1 = x_2 = 0$, see the result for $A_{\max} = 10$, $n = 76$ in Figure 6.

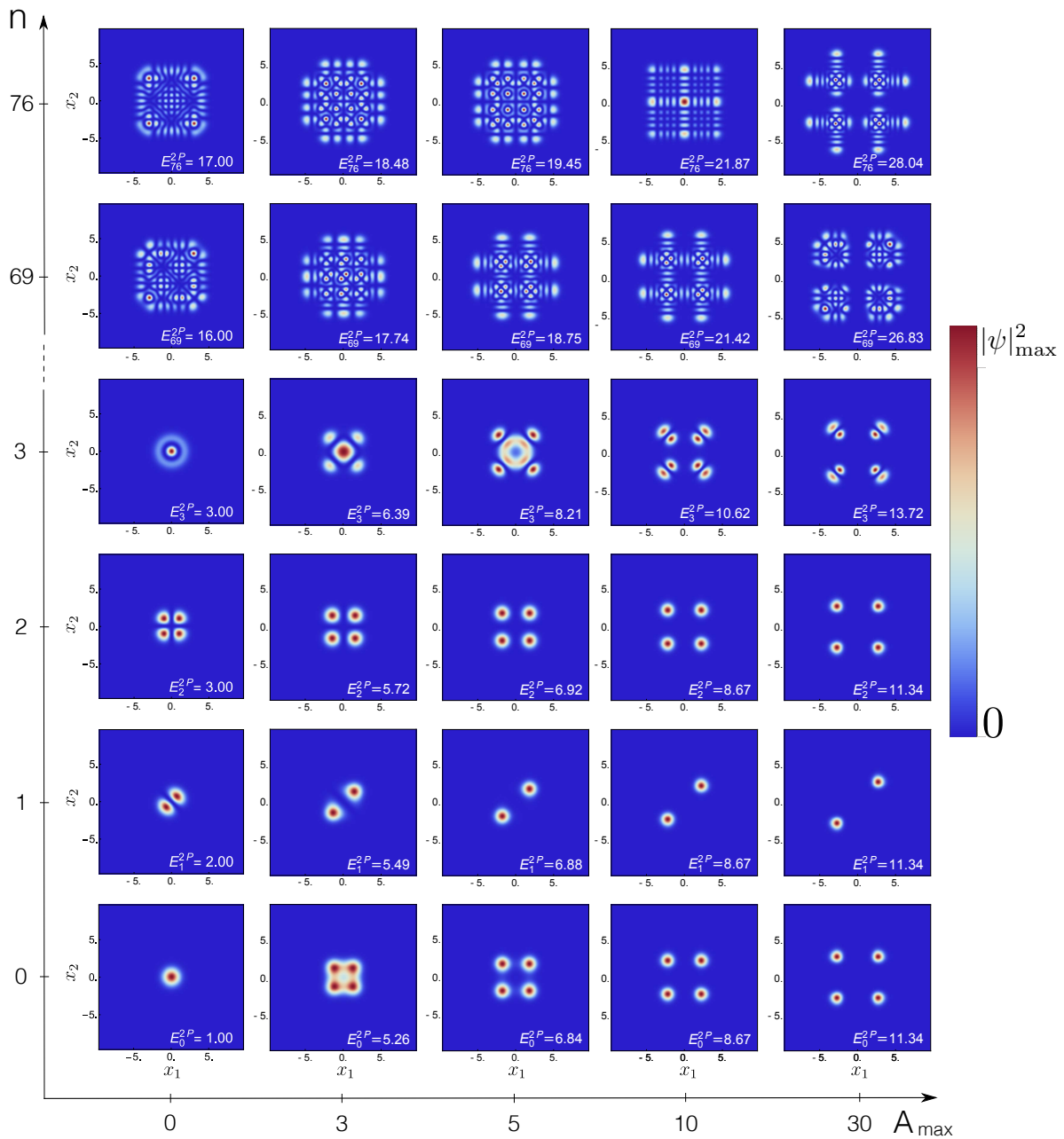


Figure 5. Probability densities $|\psi_n(x_1, x_2)|^2$ of the n th eigenstates of two non-interacting particles ($\lambda = 0$), in configuration space (x_1, x_2) , with variable barrier height from the single ($A_{\max} = 0$) to the double-well ($A_{\max} \neq 0$) scenario, cf. Equation (2). The densities are plotted on a linear scale which interpolates between vanishing probability (dark blue) and the maximum probability density $|\psi|_{\max}^2$ of the given eigenstate. FGH parameters: $x_{\max} = -x_{\min} = 40$, $N_{\text{cut}} = 330$, and $N_{\text{Grid}} = 2047$.

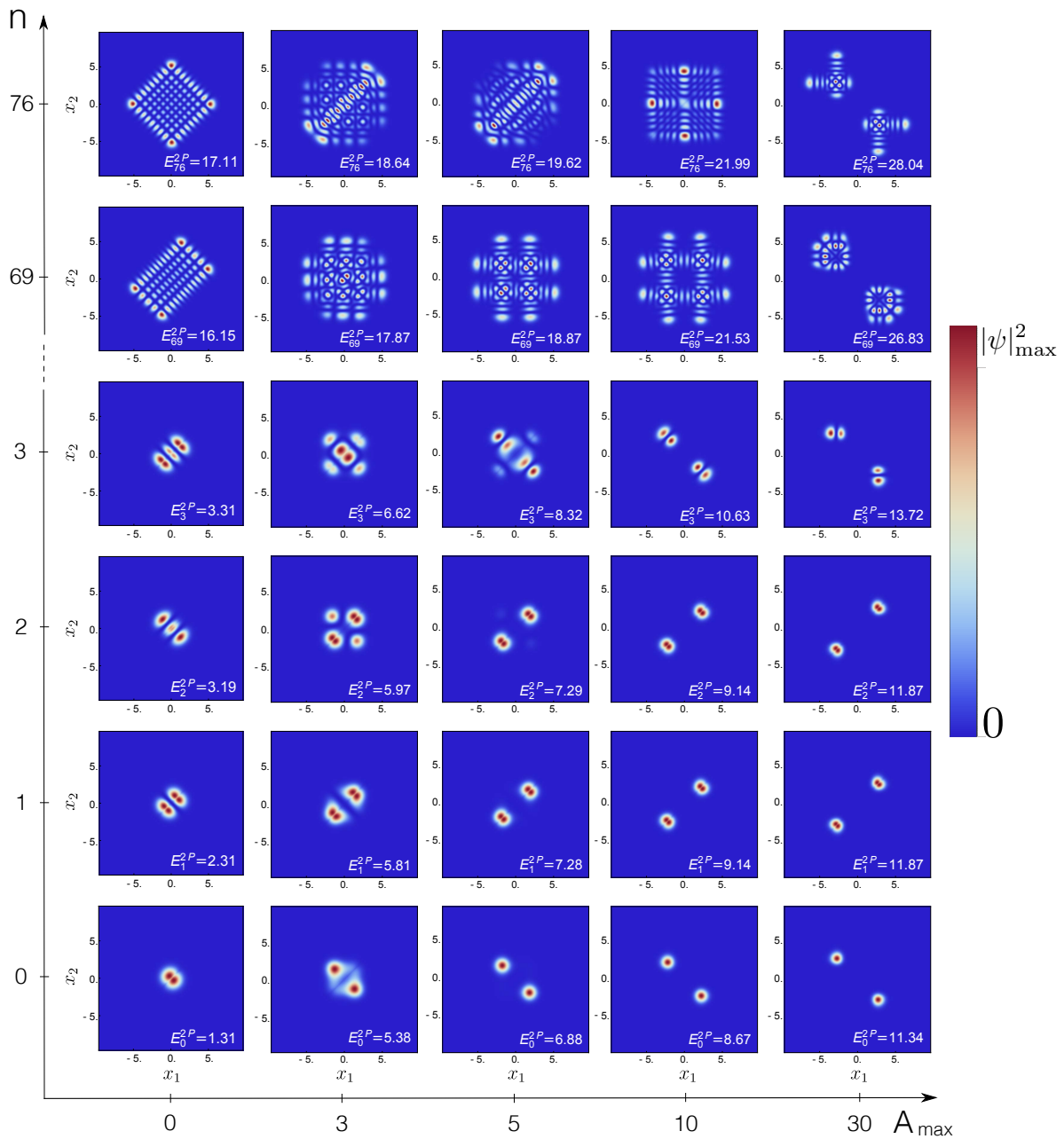


Figure 6. Probability densities $|\psi_n(x_1, x_2)|^2$ of the n th eigenstates of two interacting particles ($\lambda = 1$), in configuration space (x_1, x_2) , with variable barrier height from the single ($A_{\max} = 0$) to the double-well ($A_{\max} \neq 0$) scenario, cf. Equation (2). Color coding as in Figure 5. FGH parameters: $x_{\max} = -x_{\min} = 40$, $N_{\text{cut}} = 330$, and $N_{\text{Grid}} = 2047$.

Next, let us have a closer look at the three-body probability density $|\psi_n(x_1, x_2, x_3)|^2$ of the ground state ($n = 0$) in a deep double-well, $A_{\max} = 30$. Figure 7a,d show the three-body probability density (5) for non-interacting, $U = 0$, and interacting, $U = 1$, particles, respectively (see Equation (A21)). Since all particles occupy the same single-particle orbital $|\psi_0\rangle$, the non-interacting ground state covers all eight octants of configuration space in Figure 7a.

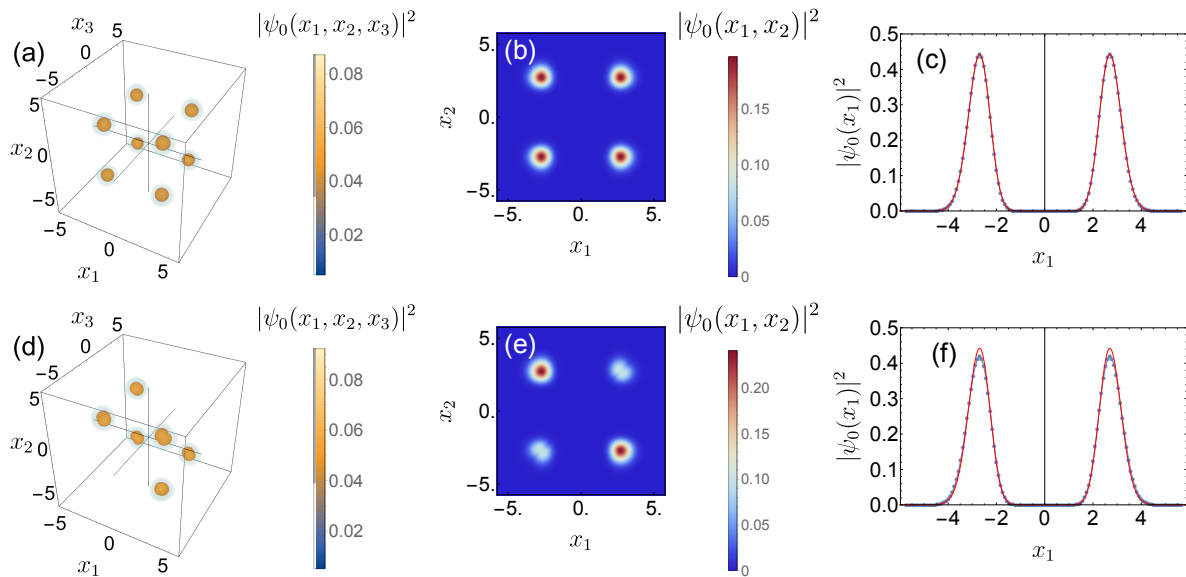


Figure 7. Three-body probability density $|\psi_0(x_1, x_2, x_3)|^2$ (a,d), diagonal of the reduced two-body probability density matrix $|\psi_0(x_1, x_2)|^2$ (b,e), and diagonal of the reduced one-body probability density matrix $|\psi_0(x_1)|^2$ (c,f) of the ground state of three (a–c) non-interacting ($U = 0$) and (d–f) interacting ($U = 1$) particles in the double-well ($A_{\max} = 30$), cf. Equation (2). Please note that in (d), $|\psi_0|^2 \approx 0$ if all bosons are in the same well ($x_1, x_2, x_3 > 0$ and $x_1, x_2, x_3 < 0$), due to the interactions. The red line in (c) is the profile of $|\psi_0(x_1)|^2$ for non-interacting particles. Parameters employed for the BH method: $x_{\max} = -x_{\min} = 10$, and $L = 231$.

Like in the two boson case, the three-body wave function develops a nodal line along the main diagonal $x_1 = x_2 = x_3$ for non-vanishing $U > 0$. At strong interaction, the maxima of the wave function are additionally shifted towards the corners of configuration space, along the diagonals $x_1 = x_2 = -x_3$, $x_1 = -x_2 = x_3$ and $-x_1 = x_2 = x_3$. Using a two-mode description, the ground state for sufficiently strong interactions is given by two particles at the same site and one on the opposite site. Therefore, the ground state, illustrated in Figure 7d, has no density in the areas associated with three particles at the same site ($x_1, x_2, x_3 > 0$ and $x_1, x_2, x_3 < 0$). Moreover, the two-mode description in the Fock basis $|n_L, n_R\rangle$ helps to understand the structure of the doubly degenerate ground state, since both states

$$\begin{aligned} |\psi_1\rangle &= |2, 1\rangle, \\ |\psi_2\rangle &= |1, 2\rangle, \end{aligned} \tag{12}$$

give rise to the same energy. The degenerate first and second excited states are then given by

$$\begin{aligned} |\psi_3\rangle &= |3, 0\rangle, \\ |\psi_4\rangle &= |0, 3\rangle, \end{aligned} \tag{13}$$

which are energetically even more sensitive to the interaction than the ground state doublet. Therefore, the four-fold degenerate ground state in the non-interacting case evolves into two doublets of states which further separate as a function of the interaction strength, as illustrated in the spectrum in Figure 4.

Finally, we inspect how the correlation information imprinted into the three-particle state is reduced when subsequently integrating out degrees of freedom. Averaging over one degree of freedom leads to the diagonal of the reduced two-body density matrix $|\psi_0(x_1, x_2)|^2 = \int dx_3 |\psi_0(x_1, x_2, x_3)|^2$, plotted for $U = 0$ and for $U = 1$ in Figure 7b,e, respectively. The impact of interaction becomes clearly visible by the reduction of the density along the diagonal $x_1 = x_2$, tantamount of reduced

correlations—as already observed in Figures 5 and 6. Please note that in some contrast to the density of the two-particle state $n = 0$, for $\lambda = 1$ and $A_{\max} = 30$ in Figure 6, the probability to detect two particles in the same well is not fully suppressed at interaction strength $U = 1$.

Averaging over the second degree of freedom leads to the diagonal of the reduced one-body density matrices, $|\psi_0(x_1)|^2 = \int dx_2 dx_3 |\psi_0(x_1, x_2, x_3)|^2$, displayed in Figure 7c,f. The profile of $|\psi_0(x_1)|^2$ for $U = 0$, cf. Figure 7c, is exactly the same as the one obtained for the non-interacting two-particle case (red line), as expected. Only a small difference between the one-body densities $|\psi_0(x_1)|^2$ associated with interacting and non-interacting (red line) bosons, respectively, is detectable, cf. Figure 7f (please note that the two-mode approximation (i.e., the double-well Bose–Hubbard model) is not sensitive to changes of the intra-well correlations—which here manifest themselves in the changed one-body density profile). This analysis therefore indicates that even if the interaction strongly affects the correlations, this information is not reflected by the one-body density profile.

4. Dynamics in the Double-Well

4.1. Static Potential: Two-Body Excited State Dynamics

Given the above phenomenology of spectra and eigenstates, we now explore how the tunneling dynamics of two interacting particles in a static double-well depends on the choice of the initial state. To this end, we consider a system initially prepared in a superposition of excited states, such that both particles are localized on the right-hand side of the double-well, at fixed barrier height $A_{\max} = 10$. This localized state can be constructed by coherent superposition of (non-interacting) adjacent, even and odd one-body eigenstates:

$$|\Psi_n^{\text{loc}}(t = 0)\rangle = \frac{1}{2} (|\Psi_{2n+1}^{1P}\rangle + |\Psi_{2n}^{1P}\rangle) \otimes (|\Psi_{2n+1}^{1P}\rangle + |\Psi_{2n}^{1P}\rangle). \tag{14}$$

The dynamics is deduced from a spectral decomposition of the many-body Hamiltonian (1) with the FGH method, and we compare the dynamics seeded by a low-lying initial state $|\Psi_{n=0}^{\text{loc}}(t = 0)\rangle$ to that of an initial state $|\Psi_{n=3}^{\text{loc}}(t = 0)\rangle$ with energy close to the potential’s saddle point, i.e., $E^{2P} \simeq 20$, see Figure 1a.

In the non-interacting case, the wave function always remains separable and, therefore, one can straightforwardly express the probabilities (8) in terms of the single-particle density, which yields

$$\begin{aligned} P_{(LL)}(t) &= P_L^2(t) = \left[\int_{x_{\min}}^0 dx |\psi(x;t)|^2 \right]^2, \\ P_{(LR)}(t) &= 2 \cdot P_L(t)P_R(t), \\ P_{(RR)}(t) &= P_R^2(t) = \left[\int_0^{x_{\max}} dx |\psi(x;t)|^2 \right]^2. \end{aligned} \tag{15}$$

Applying a simplified three-level model for $n = 0$ [65], Equation (15) can be rewritten as

$$\begin{aligned} P_{(LL)}(t) &= \sin^4\left(\frac{\Delta}{2}t\right), \\ P_{(LR)}(t) &= \frac{1}{2} \sin^2(\Delta t), \\ P_{(RR)}(t) &= \cos^4\left(\frac{\Delta}{2}t\right). \end{aligned} \tag{16}$$

Due to the equidistance between the low-lying energies E_2^{2P} , E_1^{2P} , and E_0^{2P} for $\lambda = 0$, the uncorrelated tunneling dynamics is governed by a single Rabi frequency $\Delta = E_2^{2P} - E_1^{2P} = E_1^{2P} - E_0^{2P}$ [43,44]. In

particular, for $A_{\max} = 10$, $P_{(LL)}(t)$ and $P_{(RR)}(t)$ oscillate with the period $T(\lambda = 0) = 2\pi/\Delta \simeq 12 \cdot 10^3$. In the non-interacting case, tunneling is thus a first-order single-particle process.

A finite interaction strength perturbs the equidistance between the low-lying energies and, therefore, two distinct periods emerge from the dynamics: $T_{21} = 2\pi/(E_2^{2P} - E_1^{2P})$ and $T_{10} = 2\pi/(E_1^{2P} - E_0^{2P})$, in qualitative agreement with experimental observations [31].

The evolution of these periods with λ , plotted in Figure 8, shows a rapid increase (decrease) of T_{21} (T_{10}) for weak interactions $\lambda < 0.5$, and a monotonous decrease of T_{21} for $\lambda > 0.5$, while T_{10} saturates at $T_{10} \simeq 3$ for $\lambda \rightarrow \infty$. Please note that for $\lambda = 0.5$, the Josephson oscillation period $T_{21} \sim 1750 \cdot T(\lambda = 0)$ is much larger than the one for non-interacting particles—but *finite*. This corresponds to the self-trapping regime [4]. Interestingly, the Josephson oscillation period T_{21} converges to the non-interacting period, $T_{21} \sim T(\lambda = 0)$, in the Tonks-Girardeau limit $\lambda \rightarrow \infty$. This effect agrees with the fermionized pair-state dynamics discussed in Refs. [43,44].

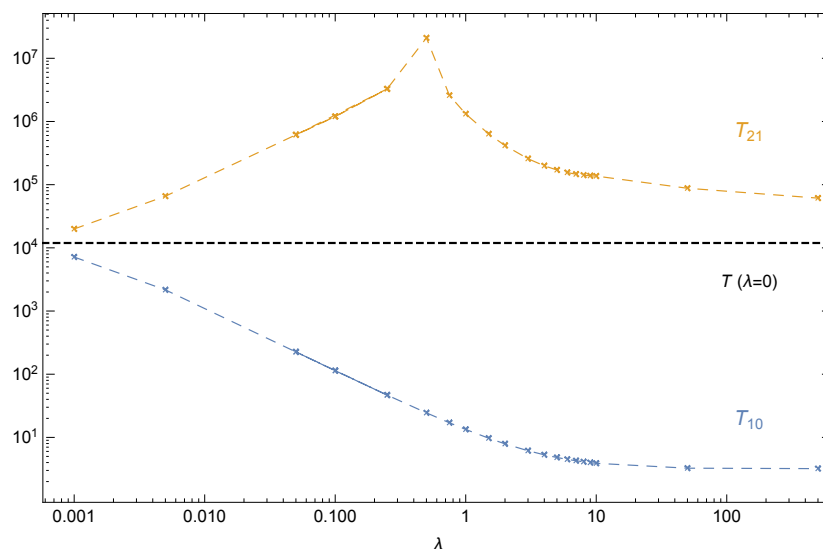


Figure 8. Characteristic periods T_{21} and T_{10} of the two-particle tunneling dynamics as displayed in Figure 9, as a function of the interaction strength λ , for a double-well potential barrier height $A_{\max} = 10$, on a double-logarithmic scale. The horizontal, black, dashed line indicates the (degenerate, see main text) period of the non-interacting case $T(\lambda = 0) \simeq 12 \cdot 10^3$.

In the two-mode approximation (i.e., the double-well Bose–Hubbard model) for the present scenario, the dynamics is fully described by the amplitudes of the Fock basis states $|n_L, n_R\rangle \in \{|2, 0\rangle, |1, 1\rangle, |0, 2\rangle\}$, with degenerate $|2, 0\rangle$ and $|0, 2\rangle$. Two correlated two-particle tunneling processes are then possible in this simplified picture: a first-order two-particle tunneling process which corresponds to the direct tunneling of both bosons along the diagonal $x_1 = x_2$ (i.e., the transition $|2, 0\rangle \rightarrow |0, 2\rangle$), or a second-order two-particle process (i.e., the transition $|2, 0\rangle \rightarrow |1, 1\rangle \rightarrow |0, 2\rangle$). We now elucidate the actual nature of the tunneling process for weak interactions.

Starting in the initial state $|\Psi_{n=0}^{\text{loc}}(t = 0)\rangle$ as defined by (14), with $\lambda = 0.005$, the dynamics clearly exhibits the Josephson oscillation period $T_{21} \simeq 65 \cdot 10^3$, garnished by a small amplitude beat frequency associated with $T_{10} \simeq 2 \cdot 10^3$. These oscillations are observed in the time evolution of the detection probabilities (8) in Figure 9a, with the Josephson oscillation period $T_{21} \simeq 5.5 \cdot T(\lambda = 0)$ strongly enhanced with respect to the non-interacting value $T(\lambda = 0)$. This is in good qualitative agreement with experimental observation [31]. One also encounters a strongly reduced probability to observe the bosons in opposite wells, signaled by $\max(P_{(LR)}) < 0.1$ in Figure 9a. The reduction of $\max(P_{(LR)})$, arising from the interaction between the particles, suggests a direct tunneling along the diagonal $x_1 = x_2$, i.e., a first-order tunneling process. Such a reduction, which is a corollary of $P_2(t) \equiv \int_{x_1 \cdot x_2 \geq 0} dx_1 dx_2 |\psi(x_1, x_2; t)|^2 = P_{(LL)}(t) + P_{(RR)}(t) = 1 - P_{(LR)}(t) \lesssim 1$, was previously discussed in

Refs. [43,44]. However, its interpretation as evidence of first-order tunneling is in contradiction with the time dependence of the integrated probability current $J_{(RR \rightarrow LR)}(t)$ also shown in Figure 9a, which clearly indicates a transport across the domain (LR). Indeed, $J_{(RR \rightarrow LR)}(t)$ records all probability which passes (LR) and *excludes* the tunneling along the diagonal $x_1 = x_2$. This quantity thus allows us to discriminate sharply the two types of two-particle tunneling. By virtue of Figure 9a, $J_{(RR \rightarrow LR)}(t) \sim P_{(LL)}(t)$ implies that almost all probability that oscillates between regions (LL) and (RR) passes region (LR). This confirms a second-order rather than a direct first-order two-particle tunneling process from region (LL) to (RR).

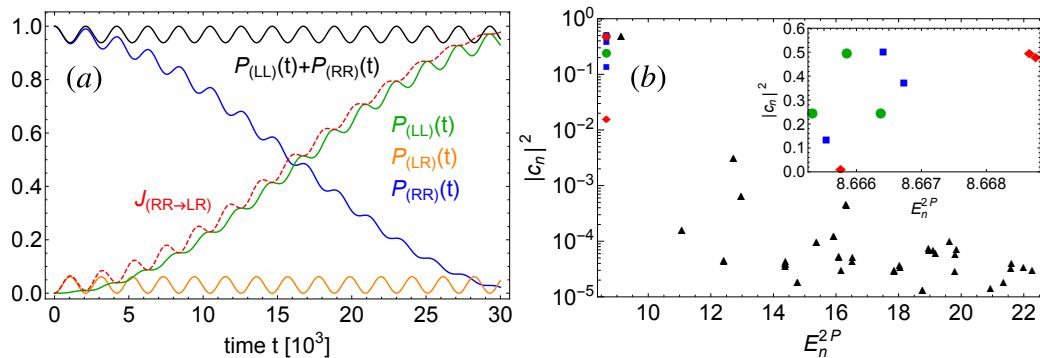


Figure 9. (a) Detection probabilities, Equation (8), and time-integrated probability current, Equation (9), as a function of time, for the two-particle initial state $|\psi_{n=0}^{\text{loc}}(t=0)\rangle$, Equation (14), and a weak interaction strength $\lambda = 0.005$. (b) Expansion coefficients of the initial state in the interacting two-body eigenbasis, as a function of the eigenenergy E_n^{2P} , for interactions $\lambda = 0$ (circles), 0.001 (squares), 0.005 (diamonds) and 1 (triangles). The inset zooms onto the dominant expansion coefficients. FGH parameters: $x_{\max} = -x_{\min} = 40$, $N_{\text{cut}} = 330$, and $N_{\text{Grid}} = 2047$.

An explanation of the underlying mechanism follows from the expansion coefficients of $|\Psi_{n=0}^{\text{loc}}(t=0)\rangle$ in the interacting two-particle basis. The inset in Figure 9b shows that for non-interacting particles, only three coefficients—associated with equidistant energies—are non-zero, giving rise to the single frequency $\Delta = E_2^{2P} - E_1^{2P} = E_1^{2P} - E_0^{2P}$ oscillations described above. Turning on a weak interaction (e.g., $\lambda \leq 0.005$, in Figure 9a), the initial state's overlap with the ground state decreases, while at the same time, the coefficients of the first two excited states pick up comparable weights (squares and diamonds in the inset). The mechanism behind the observed tunneling process is straightforward: in the previous Section, we showed that the first two excited states stick together to form a doublet with an energy which increases with λ , while the energy of the ground state—one particle localized on each well—does not depend on the interaction, cf. Figure 3. Therefore, the ground state corresponding to a balanced population in region (LR), see Figure 6, becomes off-resonant. Thus, if a boson tunnels from the right- to the left-hand side, it can populate the ground state only for very short times. The associated timescale is determined by the energy gap between the ground state and the degenerate excited states' energy. Subsequently, the boson tunnels either back to the right well, or the other boson tunnels from the right to the left well, to re-establish energy conservation. It follows from this latter argument that the involved frequencies can be inferred from a three-level model [65]. Increasing further the interaction, the excited states turn resonant with the next higher-lying band (recall Figures 2b and 3), such that additional transitions kick in, and the tunneling dynamics exhibits more frequencies, with no simple representation in the above three-level model. In terms of the expansion coefficients, this boils down to an increasing number of contributing eigenstates as illustrated, for $\lambda = 1$, by the triangles in Figure 9b.

Considering now the non-interacting, excited initial state $|\psi_{n=3}^{\text{loc}}(t=0)\rangle$ (see Equation (14)) with energy close to the saddle point, i.e., $E^{2P} \simeq 20$, the uncorrelated tunneling dynamics (not shown) is that of a separable wave function with a single Rabi frequency $\Delta = E_{59}^{2P} - E_{52}^{2P} = E_{52}^{2P} - E_{51}^{2P}$, and period $T(\lambda = 0) = 2\pi/\Delta \simeq 19.5$. This monochromaticity again is a consequence of the equidistant level

spacing of the high-lying energies E_{59}^{2P} , E_{52}^{2P} , and E_{51}^{2P} , for $\lambda = 0$ (see circles inset Figure 10b). Please note that the Rabi period $T \simeq 19.5$ is much smaller than the one observed for the initial condition $|\psi_{n=0}^{\text{loc}}(t=0)\rangle$, for which $T \simeq 12 \cdot 10^3$, since $E_{52}^{2P} - E_{51}^{2P} > E_1^{2P} - E_0^{2P}$, and the detection probabilities, Equation (8), oscillate with reduced amplitude (smaller than 1), due to a less pronounced localization of $|\psi_{n=3}^{\text{loc}}(t=0)\rangle$ in either one of the individual wells.

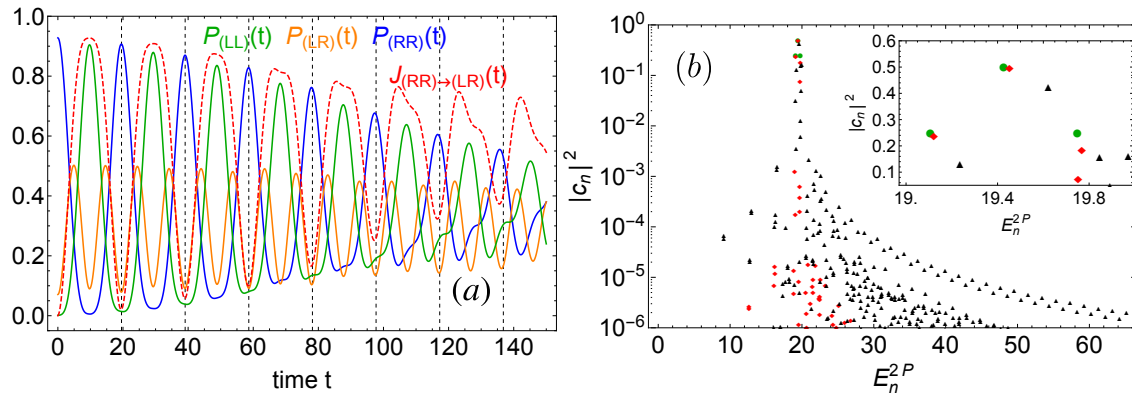


Figure 10. (a) Detection probabilities (8), and time-integrated probability current (9), as a function of time, with initial two-particle state $|\Psi_{n=3}^{\text{loc}}(t=0)\rangle$, Equation (14), and interaction strength $\lambda = 0.1$. The vertical, dashed black lines indicate the period $T(\lambda = 0) \simeq 19.5$ of the non-interacting case. (b) Expansion coefficients of the initial state in the interacting two-body eigenbasis, as a function of the eigenenergy E_n^{2P} , for interaction strengths $\lambda = 0$ (circles), 0.1 (diamonds), and 1 (triangles). The inset zooms onto the dominant expansion coefficients. FGH parameters: $x_{\text{max}} = -x_{\text{min}} = 40$, $N_{\text{cut}} = 330$, and $N_{\text{Grid}} = 2047$.

How do interactions affect the evolution of the initial state $|\Psi_{n=3}^{\text{loc}}(t=0)\rangle$? As expected from our above spectral analysis, much stronger interactions than $\lambda = 0.005$ must be considered to induce visible effects in the dynamics, since the impact of interactions is comparable for all eigenstates (cf. Figure 6, for $A_{\text{max}} = 30$ and $n = 76$) which exhibit a large overlap with the initial state. Figure 10a shows the time evolution of the detection probabilities (8) for $\lambda = 0.1$. The oscillation period seeded by $|\Psi_{n=3}^{\text{loc}}(t=0)\rangle$ appears to be much less sensitive to interactions than for $|\Psi_{n=0}^{\text{loc}}(t=0)\rangle$ (recall Figure 9): the oscillation periods of $P_{(LL)}(t)$ and $P_{(RR)}(t)$ almost coincide with the non-interacting period $T(\lambda = 0) \simeq 19.5$ indicated by vertical dashed lines. Nevertheless, a small shift is visible after seven periods around $t \simeq 136.5$. This small shift can be understood by inspection of the expansion coefficients of the initial state in the interacting two-body eigenbasis, Figure 10b. In contrast to $\lambda = 0$, where only three energy levels contribute to the dynamics (circles, inset Figure 10b), an interaction $\lambda = 0.1$ redistributes the amplitudes over four dominant states with a weight larger than 5% (squares, inset Figure 10b). The interactions slightly modify the energy gaps, leading to a small modification of the Josephson period, and give finite weight to one additional eigenstate, leading to a modulation of the plotted observables with period $T \simeq 394$. This additional modulation of the signal must not be confused with the damping of density oscillations as observed for large particle numbers in bosonic Josephson junctions [40,68]. As indicated by the time-integrated probability current which roughly follows $P_{(LL)}(t)$ in Figure 10a, we again witness a second-order tunneling across region (LR), instead of direct first-order tunneling along the diagonal $x_1 = x_2$. When further increasing the interaction, see, e.g., the diamonds for $\lambda = 1$ in Figure 10b, significantly more states contribute to the time evolution (not shown). The inter-particle interaction enforces mixing of the dynamics in the reduced single-particle subspace, and, accordingly, increases the single-particle entropy.

Before the investigation of the time-dependent double-well, we stress here that improved two-mode models for modeling the dynamics of interacting ultracold bosons confined in double-well potentials [69,70] are not sufficient to capture the dynamics as seeded by highly excited initial states.

Furthermore, the effective Hamiltonians in [69,70] contain strongly initial-state-dependent parameters and thus a comprehensive comparison of different initial states is considerably complicated.

4.2. Time-Dependent Double-Well Potential: From Few- to Many-Body Dynamics

We have seen in the previous sections how the barrier height affects the impact of interactions on the many-particle dynamics. We now generalize this analysis by considering a time-dependent switching of the barrier according to Equations (2) and (3), with $A_{\max} = 30$. Before this quench, the bosons are prepared in the interacting many-particle ground state of a harmonic trap. Our purpose is here to examine how the reduced one-body density matrix evolves for (quasi-)adiabatic vs. diabatic switching. Extrapolation to larger particle numbers using the MCTDH-X method relates our observations to previous studies of the splitting of a BEC by a laser sheet [34,39,71]. Please note that while quenches can be efficiently simulated with the help of the FGH method, we employ the MCTDH-X method (see Appendix C) for finite switching times, to deal with the time-dependent Hamiltonian (1).

We start with the time evolution of the many-body wave function when the tunneling barrier is suddenly quenched from $A_{\max} = 0$ to 30 (i.e., $T_{\text{ramp}} \rightarrow 0$) [35,72,73]. Figure 11a–d shows the behavior of the two-particle density for $\lambda = 1$, during the initial stage of the quench-induced dynamics. The initial wave packet is split along the diagonal $x_1 = x_2$, and spreads towards the outer edges of the double-well, until its reflection after half a period $t \simeq 1.9$. Since all the injected energy, i.e., $A_{\max} = 30$, is suddenly transferred to the two bosons, the turning point $x_{\text{turn}} \sim \pm 7.75$ in Figure 11c, where the reflection takes place, corresponds to $V(x_{\text{turn}}) \simeq A_{\max} = 30$ (see Figure 1b). We observe (not shown) that the higher the tunneling barrier A_{\max} , the longer the oscillation period. On its way back, the wave packet broadens more and more due to reflections at the central barrier. Finally, after one period $t \simeq 3.6$, Figure 11d, a large fraction is again located in the vicinity of the saddle point, which, subsequently, splits once more.

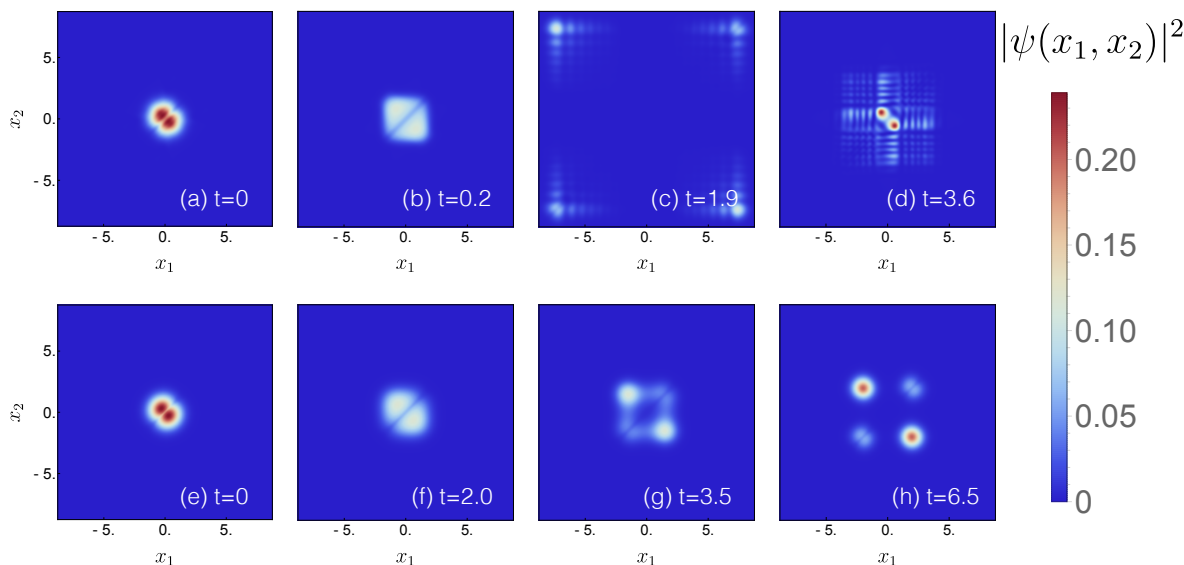


Figure 11. Time evolution of the two-body density $|\psi(x_1, x_2; t)|^2$, launched in the initial two-particle ground state of a harmonic trap, with interaction strength $\lambda = 1$, for (a–d) a diabatically switched central barrier with amplitude $A_{\max} = 30$ ($T_{\text{ramp}} \rightarrow 0$, with FGH parameters $x_{\max} = -x_{\min} = 40$, $N_{\text{cut}} = 330$, and $N_{\text{Grid}} = 2047$), and (e–h) (quasi-) adiabatic switching to $A_{\max} = 30$ ($T_{\text{ramp}} = 30$, with MCTDH-X parameters $x_{\max} = -x_{\min} = 12$, $N_x = 512$, and $M = 20$).

In contrast, for a long ramping time $T_{\text{ramp}} = 30$, see Figure 11e–h, the wave function has enough time to adapt to the new boundary conditions, such that it rather smoothly follows the minima of

the dynamically created double-well potential. The dynamics are still garnished, for this long but finite ramping time, by excitations of the first band, as identifiable by additional nodal structures in Figure 11g,h.

Comparison of the nodal structures of the two-particle densities observed in Figure 11 for $T_{\text{ramp}} = 0$ and for $T_{\text{ramp}} = 30$, respectively, suggests that less energy is absorbed by the center-of-mass degree of freedom in the latter case (as expressed by considerably fewer nodal lines, indicative of smaller momenta). To corroborate this conjecture (which is based on evidence exclusively gathered from short time dynamics), we plot the two-particle energy expectation value

$$E^{2P}(T_{\text{ramp}}) = \langle \Psi(t_0) | \mathcal{H}^{2P}(T_{\text{ramp}}) | \Psi(t_0) \rangle, \tag{17}$$

at $t_0 = 200 \gg T_{\text{ramp}}$, for variable $T_{\text{ramp}} \in [0, 30]$, in Figure 12. We observe a quick initial drop of the energy followed by a long tail approaching smoothly the energy of the ground state, for $A_{\text{max}} = 30$ and $\lambda = 1$, i.e., $E_0^{2P} \simeq 11.34$. The inset zooms into the range $T_{\text{ramp}} \in [7.5, 30.5]$, where the horizontal dashed lines indicate the eigenenergies of the two-particle system, with $A_{\text{max}} = 30$ and $\lambda = 1$. The evolution of $E^{2P}(t_0)$ implies that for $T_{\text{ramp}} \geq 19$, only transitions between the ground state and the first degenerate (recall Figure 6) excited states occur. Thus, indeed, (quasi-)adiabatic switching does perform essentially no work on the many-particle system.

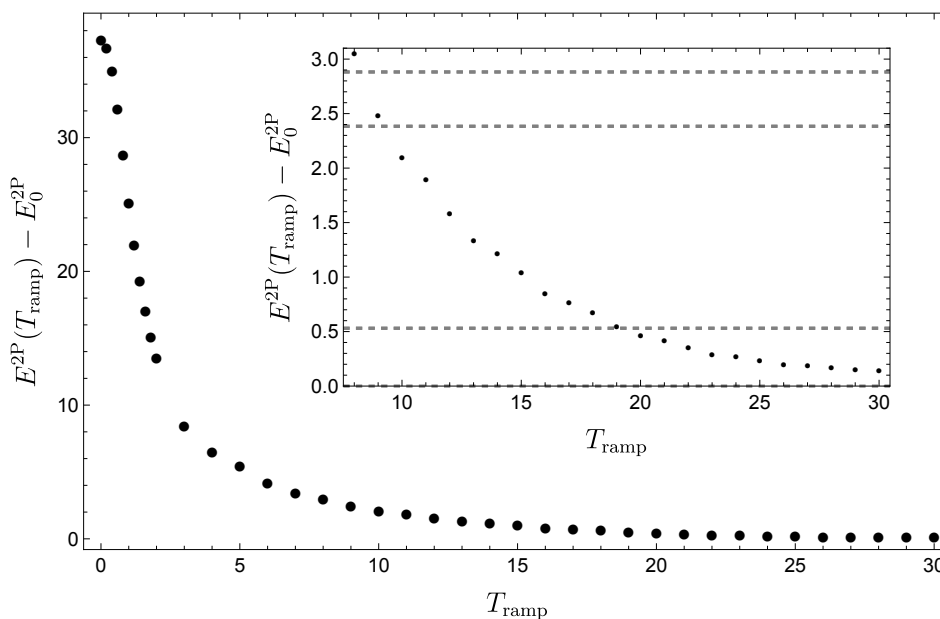


Figure 12. Two-body energy expectation, Equation (17), versus ramping time, after a fixed evolution time $t_0 = 200$, for $A_{\text{max}} = 30$ and $\lambda = 1$. The inset zooms into the range $T_{\text{ramp}} \geq 8$, where the horizontal dashed lines indicate the low-lying eigenenergies of Equation (1), computed by FGH. FGH parameters: $x_{\text{max}} = -x_{\text{min}} = 40$, $N_{\text{cut}} = 330$, and $N_{\text{Grid}} = 2047$; MCTDH-X parameters employed for the time-propagation: $x_{\text{max}} = -x_{\text{min}} = 12$, $N_x = 512$, and $M = 16$.

The static double-well’s entropy of the reduced single-particle density matrix increases from zero at $\lambda = 0$ and saturates at $\ln 2$ [37,38,56] with our definition (6) for $\lambda \rightarrow \infty, \forall A_{\text{max}}$. In our present, dynamical scenario—where the harmonic trap is split into a double-well during a time T_{ramp} —we also expect the entropy to increase with the interaction. Figure 13 shows the time evolution of the entropy for two ramping times (red/blue) and for two values of the interaction strength, (a) $\lambda = 1$ and (b) $\lambda = 0.1$.

For short ramping time, $T_{\text{ramp}} = 0.001$ (red lines), the entropy increases and saturates at ≈ 2.51 which is well below the maximal value $S^{\text{max}} = \log(M) \approx 2.77$ and which we verified with respect to the time evolution for $T_{\text{ramp}} = 0$ using the spectral decomposition based on our FGH computations

from Section 3. In agreement with the asymptotic behavior of the energy expectation value observed in Figure 12, the entropy oscillates with a single frequency for large ramping time, e.g., $T_{\text{ramp}} = 30$ (blue lines in Figure 13). The stronger the interaction, the larger the frequency as well as the offset of the minima of the entropy oscillations.

Monitoring the time evolution of the entropy over a broad interval of T_{ramp} allows us to map out the different dynamical regimes for two bosons with $\lambda = 1$ and $\lambda = 0.1$, respectively, see Figure 14a,d.

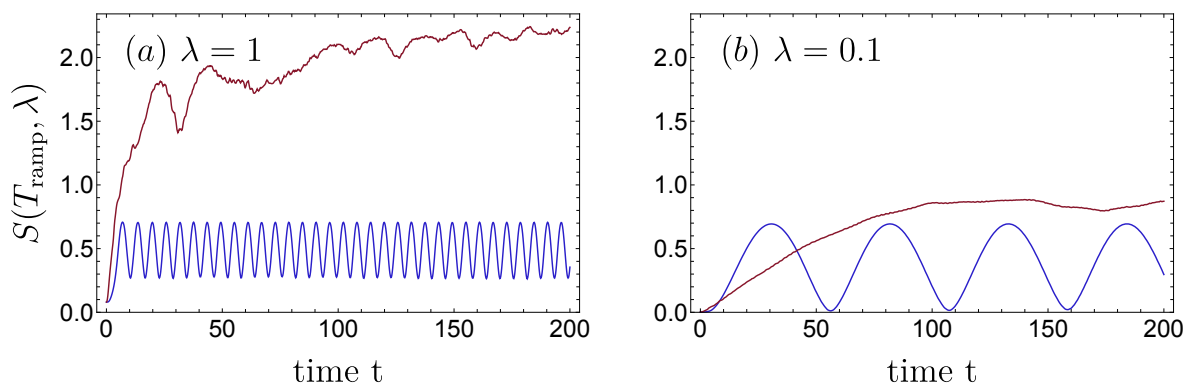


Figure 13. Von Neumann entropy (6) of the interacting two-particle state launched in the harmonic oscillator (interacting) two-particle ground state, as a function of time, for short and long ramping times, $T_{\text{ramp}} = 0.001$ (red) and $T_{\text{ramp}} = 30$ (blue), and strong ($\lambda = 1$, (a)) and weak ($\lambda = 0.1$, (b)) interaction, respectively. For small T_{ramp} , the entropy increases and finally saturates, whereas it oscillates for long ramping times. MCTDH-X parameters: $x_{\text{max}} = -x_{\text{min}} = 12$, $N_x = 512$, and $M = 16$.

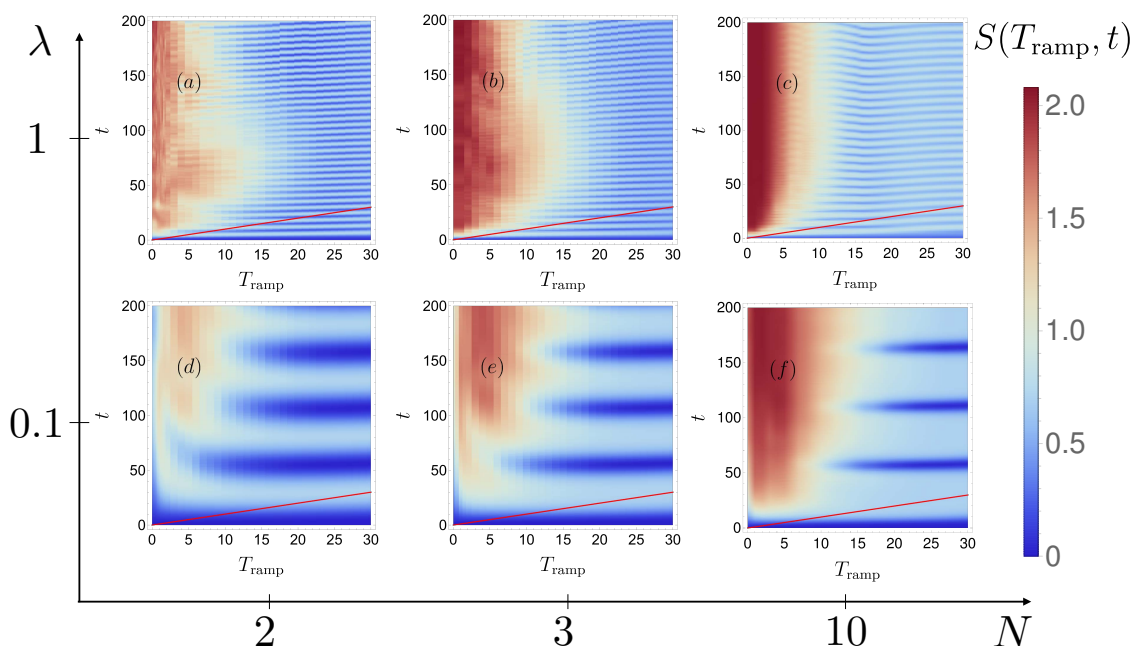


Figure 14. Time evolution of the von Neumann entropy $S(T_{\text{ramp}}, t)$, Equation (6), as a function of the ramping time T_{ramp} , for a final barrier height $A_{\text{max}} = 30$, increasing particle number $N = 2, 3, 10$ (from left to right), and interaction strengths $\lambda = 1$ (a–c) and $\lambda = 0.1$ (d–f). The red line indicates the full switching duration $t = T_{\text{ramp}}$ for the ramp to reach its maximum (Parameter values employed in the MCTDH-X calculation: $x_{\text{max}} = -x_{\text{min}} = 12$, $N_x = 512$, $M = 8$).

In full agreement with what we observed above for the dependence of the energy expectation value on T_{ramp} , the transition from diabatic to (quasi-)adiabatic dynamics is also here the primary

feature: For short ramping times, the entropy rapidly saturates at its equilibrium value, whereas, for a sufficiently slow ramp, an oscillation emerges, with a single, well-defined frequency (and decreasing amplitude, for increasing T_{ramp}). A discrete Fourier transform of the signal for $T_{\text{ramp}} \approx 19 - 30$ shows that this frequency is determined by the energy gap (see Section 3.1) between the ground and first excited state,

$$\nu(\lambda) = \frac{E_1^{2P}(\lambda) - E_0^{2P}}{\pi}. \quad (18)$$

Indeed, only two eigenstates of the reduced single-particle density matrix—with opposite parity and densities which closely resemble the typical structure of the double-well ground state doublet [56]—contribute to the dynamics in this oscillating region (not shown). For intermediate ramping times ($T_{\text{ramp}} \approx 10 - 19$), the structures observed in Figure 14a,d still express the switching-induced, coherent coupling of more than just two interacting eigenstates, because in this regime the dynamics are not yet (quasi-) adiabatic (in agreement with our discussion of Figure 12).

Remarkably, although the detailed spectral structures are rather different for two and three particles (see Figures 3 and 4), the ramping-induced time dependence of the von Neumann entropy is qualitatively similar for $N = 2, 3$, and even $N = 10$ (where we cannot access the spectral structure, with our presently available numerical resources) see Figure 14a–c, for $\lambda = 1$, and Figure 14d–f, for $\lambda = 0.1$. We attribute this feature to the coarse-graining effect of a diabatic switch, where only the effective density of states must be gauged against the spectral width of the time-dependent perturbation. Closer inspection suggests that efficient excitation is achieved for slightly longer switching times with increasing particle number, which is consistent with the increase of the density of states with N . The frequency $\nu \sim E_1^{\text{NP}} - E_0^{\text{NP}}$ of the entropy oscillations slowly decreases with the number of particles, since the energy gap $\Delta E = E_1^{\text{NP}} - E_0^{\text{NP}}$ between the first excited state and the ground state decreases with N , i.e., $\Delta E(N = 2) > \Delta E(N = 10)$. Also note that the oscillating regime of Figure 14c,f corresponds to the two-fold fragmented BEC discussed in Refs. [34,39,40]. Similar results are observed for different barrier heights (not shown) [56].

Let us conclude this section with a remark on the convergence of the MCTDH-X results reported in Figure 14c,f: For moderate and large $T_{\text{ramp}} \gtrsim 7$, only two orbitals of the employed $M = 8$ orbitals have a significant population and the entropy S remains significantly smaller than the maximal value $S^{\text{max}} = \log(M)$. From this fact it can be inferred that the wave function is accurately described in these MCTDH-X computations at $T_{\text{ramp}} \gtrsim 7$. However, for small ramping times ($T_{\text{ramp}} \lesssim 7$) all $M = 8$ employed orbitals in the computation were populated. Consequently, the entropy reaches its maximum S^{max} . This maximal entropy for small T_{ramp} implies that the Hilbert space provided by MCTDH-X is not large enough to host the complete dynamics of the many-body wave functions and more orbitals ($M > 8$) would therefore be necessary to achieve convergence. Based on the FGH results for sudden switches of the potential barrier, to cover the subspace of the Hilbert space more than $M = 16$ (corresponding to a maximal entropy of $S^{\text{max}} \approx 2.77$) orbitals are necessary, which exceeds the typically employed number of orbitals ($M \in \{12 \dots 16\}$) for $N \leq 10$ bosons reported in the literature [74,75]. While the quantitative behavior of the entropy $S(T_{\text{ramp}}, t)$ at small $T_{\text{ramp}} \lesssim 7$ in Figure 14c,f therefore cannot be considered fully converged, the observed behavior is qualitatively equivalent to that resulting for smaller particle numbers, where convergence of MCTDH-X could be achieved with a smaller number $M = 2, 4, 6$ of orbitals, and is also consistent with our FGH-based analysis for $N = 2$ particles (see Figure 12). This suggests that the results reported in Figure 14c,f correctly indicate the qualitative trend of the evolution also for short ramping times.

5. Conclusions

We analyzed the spectral structures and the dynamics of a few interacting bosons in a one-dimensional double-well potential, for both a static and a time-dependent potential barrier, beyond the two-mode approximation. To this end, we used three complementary numerical methods.

The Fourier Grid Hamiltonian method was employed to extract the full spectral information for two interacting bosons, whereas a Bose–Hubbard representation of the continuous double-well potential was found to be more efficient to describe the spectral structure of the three-particle case. Furthermore, we used the MCTDH-X method to simulate the dynamical evolution of $N = 2, 3$, and 10 interacting bosons in a potential with time-dependent barrier strength.

Our spectral analysis highlights the dependence of the energy spectrum on the interaction strength, on the one hand, and on the potential barrier height, on the other. Ramping up a barrier in the center of an initially harmonic potential introduces a metamorphosis of state space from a simple, highly degenerate harmonic oscillator progression, into a sequence of states which exhibit the characteristic degeneracies associated with tunneling between symmetric wells, below the barrier energy, and a harmonic-like spectrum sufficiently high above the barrier, separated by a range around the barrier energy which mediates between both classes. Interactions lift many of the energetic degeneracies and eventually induce mixing of energetic manifolds which otherwise remain well-separated.

While for two (on-site interacting) particles distributed over two (deep) wells eigenstates exist which remain unaltered by finite interactions, this is no longer true for three particles in the same potential, since at least two particles then must interact: two manifolds of states emerge corresponding to states where two or three particles are interacting. We supplemented our spectral analysis by inspecting many-particle probability densities in configuration space, which directly exhibit the spatial correlations inscribed into the many-body tunneling dynamics, for both energetically low- and high-lying states. For three particles, we visualized the loss of information about correlations when tracing from the three-body density to the two-body, and, eventually, to the one-body density.

We used that spectral information to decipher the tunneling dynamics of two interacting particles in a static double-well. In particular, we compared and characterized Josephson oscillations of two interacting bosons prepared in a superposition of excited states with energies either well below or close to the potential's saddle point. Inspection of the expansion coefficients of the evolved two-particle state in the interacting two-particle basis provided evidence that a simple three-level description of the dynamics fails at sufficiently strong interactions. The Josephson period at energies close to the saddle point is much smaller and robust with respect to the interaction. In agreement with observations in Ref. [31], we confirm a second-order pairwise tunneling process.

Finally, we investigated the spreading behavior of the many-particle state, when initially prepared in the many-particle harmonic oscillator ground state, under diabatic vs. (quasi-) adiabatic switching of a central barrier—transforming the potential into a double-well. Diabatic switching leads to efficient energy transfer through the population of many many-particle excited states, as quantified by the time evolution of the von Neumann entropy of the reduced single-particle density matrix, while a (quasi-) adiabatic ramp only populates weakly excited states. This phenomenology emerges already for two interacting particles and—due to the increasing spectral density—gets more pronounced for ten particles, the largest particle number here considered.

Author Contributions: All authors contributed equally to the manuscript. All authors have read and agreed to the published version of the manuscript.

Funding: We acknowledge support through the EU collaborative Project QuProCS (Grant Agreement 641277), as well as by the state of Baden-Württemberg through bwHPC (NEMO and JUSTUS clusters). FS acknowledges financial support by the Swiss National Science Foundation (SNSF) and the NCCR Quantum Science and Technology. LdFdP acknowledges the Alexander von Humboldt-Foundation for financial support. MABM acknowledges financial support from CONACyT postdoctoral fellowship program. AUJL acknowledges financial support by the Austrian Science Foundation (FWF) under grant P32033 and computation time at the Hazel Hen cluster at the HLRS Stuttgart.

Acknowledgments: We would like to thank Gabriel Dufour for inspiring discussions and a careful reading of the manuscript.

Conflicts of Interest: The authors declare no conflict of interest.

Appendix A. Fourier Grid Hamiltonian Method

The FGH method [76,77] is a special case of a discrete variable representation where the eigenfunctions of the single-particle Hamiltonian are computed directly as the amplitudes of the wave function on the grid points. The results of the FGH method—the single-particle eigenenergies and eigenstates—are then used as a basis set representation of the many-particle Hamiltonian. A subsequent exact diagonalization determines the many-body spectrum.

The FGH numerical implementation requires a discretization of the continuous coordinate space by a discrete set of an odd number of N_{Grid} lattice points distributed in a uniform manner, such that $x_m = x_{\text{min}} + m\Delta x$, with $m \in [0, N_{\text{Grid}} - 1]$. This discretization leads to a grid and momentum spacing

$$\Delta x = \frac{x_{\text{max}} - x_{\text{min}}}{N_{\text{Grid}}}, \quad (\text{A1})$$

$$\Delta p = \frac{2\pi}{x_{\text{max}} - x_{\text{min}}}. \quad (\text{A2})$$

From Equation (1), the single-particle Hamiltonian matrix elements $\mathcal{H}_{mn} = \langle x_m | \mathcal{H} | x_n \rangle$ read [76]

$$\begin{aligned} \mathcal{H}_{mn} &= \sum_{l=1}^{\frac{N_{\text{Grid}}-1}{2}} \frac{(l\Delta p)^2}{\Delta x N_{\text{Grid}}} \cos\left(\frac{2\pi l(m-n)}{N_{\text{Grid}}}\right) \\ &+ \frac{V(x_m, t)}{\Delta x} \delta_{mn}, \end{aligned} \quad (\text{A3})$$

with the potential $V(x_m, t)$ defined by Equation (2). Using this discretized procedure, the wave function may be represented as a vector on a discretized grid of points

$$|\Psi\rangle = \Delta x \sum_m \psi_m |x_m\rangle, \quad (\text{A4})$$

with $\psi_m = \psi(x_m) = \langle x_m | \Psi \rangle$ the value of the wave function evaluated at x_m , and with orthogonality condition $\Delta x \langle x_m | x_n \rangle = \delta_{mn}$.

We thus obtain a discretized position representation of the single-particle Hamiltonian and must compute the eigenvalues of this Hamiltonian matrix. To this end, we consider the energy expectation value with respect to state $|\psi\rangle$, given by

$$E = \frac{\langle \Psi | \mathcal{H} | \Psi \rangle}{\langle \Psi | \Psi \rangle} = \frac{\sum_{mn} \psi_m^* \Delta x \mathcal{H}_{mn} \psi_n}{\sum_m |\psi_m|^2}. \quad (\text{A5})$$

The minimization of this energy functional by variation of the coefficients ψ_m leads to the secular equations

$$\begin{aligned} \sum_{n=0}^{N_{\text{Grid}}-1} \left[\Delta x \mathcal{H}_{mn} - E_m^{1P} \delta_{mn} \right] \psi_n &= 0, \\ m &= 0, \dots, N_{\text{Grid}} - 1, \end{aligned} \quad (\text{A6})$$

with eigenvalues E_m^{1P} . The eigenvectors $|\Psi_m\rangle$ give directly the (approximate) values of the solutions of the Schrödinger equation evaluated at the grid points. As discussed below, the convergence of the method in the absence of free scattering states is, a posteriori, well controlled, thus leading to a *numerically exact* result, i.e., with an error of the order of machine precision. Furthermore, since the single-particle Hamiltonian is real and symmetric, these eigenstates can always be chosen to be real. Please note that the double-well potential investigated does not exhibit free scattering solutions, but only bound states.

The precision of the FGH method can be enhanced by varying two characteristic parameters: (1) The range $x_{\max} - x_{\min}$ determines the maximum value of the potential $V_{\max}(x_{\max}, t)$. As soon as the energy of a given bounded state $|\Psi_n\rangle$ does not exceed the truncation $V_{\max}(x, t)$, convergence can be controlled. For instance, with $x_{\max} = -x_{\min} = 40$ and $A_{\max} \lesssim 30$, roughly the $N_{\text{cut}} = 600$ lowest-lying energy eigenstates can be converged with a precision up to 10^{-9} . (2) Increasing the number of grid points N_{Grid} within a fixed range $x_{\max} - x_{\min}$ improves the accuracy of the eigenenergies of the N_{cut} states toward the exact solutions. Typically, with $x_{\max} = -x_{\min} = 40$ and $N_{\text{cut}} = 330$, we used $N_{\text{Grid}} = 2047$. These parameters ensure an energy convergence up to 10^{-9} in natural units and satisfy the orthonormality $\langle \Psi_n | \Psi_m \rangle = \delta_{nm}$ of the generated eigenstates, to machine precision.

Using second quantization, the two-body Hamiltonian, expressed in terms of the single-particle eigenbasis obtained from the FGH method, reads

$$\mathcal{H}^{2P} = \sum_{k=0}^{N_{\text{cut}}-1} E_k^{1P} \hat{n}_k + \frac{1}{2} \sum_{ksql=0}^{N_{\text{cut}}-1} W_{ksql} \hat{a}_k^\dagger \hat{a}_s^\dagger \hat{a}_q \hat{a}_l, \tag{A7}$$

with \hat{a}_k^\dagger (\hat{a}_k) the creation (annihilation) operator in state k , and where $\hat{n}_k = \hat{a}_k^\dagger \hat{a}_k$ counts the number of particles in state k . The matrix element W_{ksql} originates from contact interactions. The Hamiltonian matrix, of dimension

$$\dim(\mathcal{H}^{2P}) = \frac{N_{\text{cut}}(N_{\text{cut}} + 1)}{2}, \tag{A8}$$

is computed in the Hilbert space of symmetrized and normalized two-body states $|\Psi_n \Psi_m\rangle$, constructed from the single-particle product states such that

$$|\Psi_n \Psi_m\rangle \equiv \frac{|\Psi_n\rangle \otimes |\Psi_m\rangle + |\Psi_m\rangle \otimes |\Psi_n\rangle}{\sqrt{2} \sqrt{1 + \langle \Psi_n | \Psi_m \rangle}}, \tag{A9}$$

for $N_{\text{cut}} \geq n \geq m \geq 1$. Using this two-particle basis, the diagonal Hamiltonian matrix elements read

$$\langle \Psi_n \Psi_m | \sum_{k=0}^{N_{\text{cut}}-1} E_k^{1P} \hat{n}_k | \Psi_{n'} \Psi_{m'} \rangle = (E_n^{1P} + E_m^{1P}) \delta_{nn'} \delta_{mm'}, \tag{A10}$$

whereas the off-diagonal interaction terms read

$$\begin{aligned} & \frac{1}{2} \sum_{ksql=0}^{N_{\text{cut}}-1} W_{ksql} \langle \Psi_n \Psi_m | \hat{a}_k^\dagger \hat{a}_s^\dagger \hat{a}_q \hat{a}_l | \Psi_{n'} \Psi_{m'} \rangle \\ &= \begin{cases} W_{nnn'n'}, & \text{for } n = m, n' = m', \\ \sqrt{2} W_{nnn'm'}, & \text{for } n \neq m, n' = m', \\ \sqrt{2} W_{mnn'm'}, & \text{for } n = m, n' \neq m', \\ 2W_{mnn'n'}, & \text{for } n \neq m, n' \neq m', \end{cases} \end{aligned} \tag{A11}$$

with

$$W_{ksql} = \lambda \sum_{m=0}^{N_{\text{Grid}}-1} \Delta x \psi_m^k \psi_m^s \psi_m^q \psi_m^l \tag{A12}$$

numerically calculated using a Kahan summation algorithm [78] to minimize the accumulated numerical error.

Then, the Hamiltonian matrix is diagonalized with MATHEMATICA's build-in LAPACK-routines and MKL parallelization feature, which ultimately determine several $\dim(\mathcal{H}^{2P})$ eigenvalues E_n^{2P} and

associated eigenvectors $|\Psi_n^{2P}\rangle$. The time evolution of the interacting two-particle system is given by the spectral decomposition

$$|\Psi(t)\rangle = \sum_{n=0}^{\dim(\mathcal{H}^{2P})-1} e^{-itE_n^{2P}} \langle \Psi_n^{2P} | \Psi(t=0) \rangle |\Psi_n^{2P}\rangle, \tag{A13}$$

with initial state $|\Psi(t=0)\rangle$.

Appendix B. Bose–Hubbard Model in the Continuum

The discretization of the continuous configuration space as performed hereafter ultimately leads to a Hamiltonian which exhibits the familiar structure of a Bose–Hubbard Hamiltonian, amended by a site-dependent potential form. Therefore, the model developed below is referred to as the Bose–Hubbard (BH) model in the continuum [79]. This approach gives access to the energy spectrum of two and three interacting bosons with a good accuracy. The main advantage of this technique is that its convergence weakly depends on the interaction strength, which is not the case with the FGH method for which the matrix to diagonalize is dense in the presence of interactions, then introducing high CPU time and memory costs.

Starting from the generic many-body Hamiltonian for N ultracold particles in the continuum limit, with contact interactions and double-well potential $V(x, t)$ (Equation (2)),

$$\begin{aligned} \mathcal{H}^{NP} &= \int dx \hat{\Psi}^\dagger(x) \left[-\frac{1}{2} \frac{\partial^2}{\partial x^2} + V(x, t) \right] \hat{\Psi}(x) \\ &+ \frac{\lambda}{2} \int dx \hat{\Psi}^\dagger(x) \hat{\Psi}^\dagger(x) \hat{\Psi}(x) \hat{\Psi}(x), \end{aligned} \tag{A14}$$

we use the single-band description. For practical implementation aspects, the continuous space is artificially discretized by covering it with Wannier functions. We can then expand the field operators $\hat{\Psi}(x)$ in the basis of localized and orthonormal Wannier functions of the lowest-lying band $w_0(x - x_i)$:

$$\hat{\Psi}(x) = \sum_{i=1}^L \hat{a}_i w_0(x - x_i), \tag{A15}$$

with \hat{a}_i the annihilation operator for a particle in the single-mode Wannier function $w_0(x - x_i)$ at site i , and L the number of sites in the discretization (assimilable to the number of grid points in the FGH method). Inserting the expansion (A15) in Equation (A14), we obtain

$$\begin{aligned} \mathcal{H}^{NP} &= -\frac{1}{2} \sum_{ij} \int dx \hat{a}_i^\dagger w_0^*(x - x_i) \frac{\partial^2}{\partial x^2} \hat{a}_j w_0(x - x_j) \\ &+ \sum_i \hat{n}_i V(x_i, t) \\ &+ \frac{\lambda}{2} \sum_i \hat{n}_i (\hat{n}_i - 1) \int dx |w_0(x - x_i)|^4, \end{aligned} \tag{A16}$$

where $\hat{n}_i = \hat{a}_i^\dagger \hat{a}_i$ and $\hat{n}_i (\hat{n}_i - 1) = \hat{a}_i^\dagger \hat{a}_i^\dagger \hat{a}_i \hat{a}_i$.

Then, the kinetic term is discretized by a finite lattice spacing $\delta_x = (2x_{\max}) / (L - 1)$,

$$\frac{\partial^2}{\partial x^2} \hat{a}_j w_0(x - x_j) \simeq \frac{1}{\delta_x^2} \hat{a}_{j+1} w_0(x - x_{j+1}) \tag{A17}$$

$$+ \frac{1}{\delta_x^2} \hat{a}_{j-1} w_0(x - x_{j-1}) \tag{A18}$$

$$- \frac{2}{\delta_x^2} \hat{a}_j w_0(x - x_j), \tag{A19}$$

such that L grid points are uniformly distributed between $x_{\min} = -x_{\max}$ and x_{\max} , and the discretized Wannier function reads

$$w_0(x - x_i) \rightarrow w_{0i}/\sqrt{\delta_x}. \quad (\text{A20})$$

With the on-site interaction strength

$$U \equiv \lambda \sum_i |w_{0i}|^4, \quad (\text{A21})$$

the BH Hamiltonian in the continuum takes the final form

$$\begin{aligned} \mathcal{H}^{NP} &= -\frac{1}{2\delta_x^2} \sum_{i=1}^{L-1} \left(\hat{a}_i^\dagger \hat{a}_{i+1} + \hat{a}_{i+1}^\dagger \hat{a}_i \right) \\ &+ \sum_{i=1}^L \left(V_i(t) + \frac{1}{\delta_x^2} \right) \hat{n}_i \\ &+ \frac{U}{2\delta_x} \sum_{i=1}^L \hat{n}_i (\hat{n}_i - 1). \end{aligned} \quad (\text{A22})$$

The double-well potential, in accordance with Equation (2), is then encoded by the explicit form

$$\begin{aligned} V_i(t) &= \frac{x_i^2}{2} + A(t)e^{-x_i^2/2}, \\ x_i &\in \{-x_{\min}, -x_{\min} + \delta_x, \dots, x_{\max}\} \end{aligned} \quad (\text{A23})$$

which for $A(t) = 0$, turns into a harmonic (single-well) trapping potential. Using the Fock basis $|\vec{n}\rangle$, the Hamiltonian matrix elements read

$$\mathcal{H}_{mn}^{NP} = \langle \vec{m} | \mathcal{H}^{NP} | \vec{n} \rangle. \quad (\text{A24})$$

For three particles, the matrix to diagonalize has a size of

$$\dim(\mathcal{H}^{3P}) = \frac{1}{6} L(L+1)(L+2). \quad (\text{A25})$$

Despite the sparsity of the matrix—which is a great advantage compared to the FGH method—the diagonalization of this matrix is rather challenging. Indeed, for 3 particles, we have used $x_{\max} = -x_{\min} = 10$ and $L = 231$, leading to a matrix size of $2,081,156 \times 2,081,156$. To obtain parts of the spectrum with reliable degeneracies, we used the MATHEMATICA's implementation of the FEAST eigensystem solver [80] for sparse matrices, which is inspired by the contour integration and density matrix representation in quantum mechanics [81]. Within a given energy search interval $\{E_{\min}, E_{\max}\}$, the FEAST algorithm reduces the size of the eigenvalue problem to a subspace of size associated with the number of eigenvalues in this interval. This approach naturally captures the degeneracies in the energy spectrum [80]. Moreover, using MATHEMATICA, the FEAST method is MPI parallelized over all processors on a single node on the cluster.

Appendix C. Multiconfigurational Time-Dependent Hartree Method for Indistinguishable Particles

MCTDH-X allows for the investigation of interacting particles in many scenarios, e.g., interacting bosons or fermions in optical lattices [82], quantum vortex re-connections in a Bose–Einstein condensate [83], or bosons in double-well potentials [39,41,44]. In our context, this method is useful for the investigation of N interacting bosons in a time-dependent double-well potential. Nevertheless, this method is not efficient for the calculation of the entire energy spectrum, thus justifying our use of the FGH and BH methods for a few particles. In the following, we outline the basic steps towards the MCTDH-X equations of motion, see Ref. [14] for supplemental details regarding the method.

The aim is to solve the time-dependent Schrödinger equation

$$i\frac{\partial}{\partial t}|\Psi\rangle = \mathcal{H}|\Psi\rangle, \quad (\text{A26})$$

with many-body Hamiltonian \mathcal{H} defined by Equation (1). To do so, we first formulate a general multiconfigurational ansatz for the wave function based on truncating the field operator

$$\hat{\Psi}(x, t) = \sum_k \hat{a}_k(t) \phi_k(x, t) \quad (\text{A27})$$

from an infinite to a finite sum of M operators, i.e.,

$$\hat{\Psi}(x, t) \approx \sum_{k=1}^M \hat{a}_k(t) \phi_k(x, t). \quad (\text{A28})$$

Under this assumption, the bosonic ansatz for the many-body wave function reads

$$|\Psi\rangle = \sum_{\{\vec{n}\}} C_{\vec{n}}(t) \prod_{k=1}^M \frac{(\hat{a}_k^\dagger(t))^{n_k}}{\sqrt{n_k!}} |\text{vac}\rangle, \quad (\text{A29})$$

where the summation runs over all (symmetrized) basis states of the Hilbert space. The vector $\vec{n} = (n_1, n_2, \dots, n_M)$ represents the occupations of the orbitals that preserve the total number of particles $n_1 + n_2 + n_3 + \dots + n_M = N$, M is the number of orbitals $\phi_k(x, t)$, and $|\text{vac}\rangle$ is the vacuum. This (a posteriori controlled) assumption, which is the key idea of MCTDH-X, greatly reduces the computational effort.

Using this ansatz, the time-dependent Schrödinger equation is solved by using the time-dependent variational principle for minimizing the action functional [84]

$$\mathcal{S}[\{C_{\vec{n}}(t)\}, \{\phi_k(x, t)\}] = \int dt \left[\langle \Psi(t) | \left(\mathcal{H} - i\frac{\partial}{\partial t} \right) | \Psi(t) \rangle - \sum_{k,j=1}^M \mu_{kj}(t) \left(\langle \phi_k(t) | \phi_j(t) \rangle - \delta_{kj} \right) \right],$$

where the time-dependent Lagrange multipliers $\mu_{kj}(t)$ enforce the orthonormality of the orbitals.

The minimization of the action \mathcal{S} finally leads to the MCTDH-X equations of motion, i.e., a coupled set of first-order non-linear differential equations [14]

$$i\frac{\partial}{\partial t} C_{\vec{n}}(t) = \sum_{\vec{m}} \langle \vec{n}, t | \mathcal{H} | \vec{m}, t \rangle C_{\vec{m}}(t), \quad (\text{A30})$$

$$\begin{aligned} i\frac{\partial}{\partial t} |\phi_k\rangle &= \mathbf{P} \left[\left(-\frac{1}{2} \frac{d^2}{dx^2} + V(x, t) \right) |\phi_k\rangle \right. \\ &\quad \left. + \lambda \sum_{\alpha\beta\gamma\delta}^M \{\rho^{(1)}\}_{k\alpha}^{-1} \rho_{\alpha\beta\gamma\delta}^{(2)} \phi_\beta^*(x, t) \phi_\delta(x, t) |\phi_\gamma\rangle \right], \end{aligned} \quad (\text{A31})$$

where $\mathbf{P} = 1 - \sum_{j=1}^M |\phi_j\rangle \langle \phi_j|$ denotes the projection operator, and where $\rho_{k\alpha}^{(1)} = \langle \Psi | \hat{a}_k^\dagger \hat{a}_\alpha | \Psi \rangle$ and $\rho_{\alpha\beta\gamma\delta}^{(2)} = \langle \Psi | \hat{a}_\alpha^\dagger \hat{a}_\beta^\dagger \hat{a}_\gamma \hat{a}_\delta | \Psi \rangle$ are respectively the matrix elements of the reduced single- and two-particle density matrices. The projector \mathbf{P} vanishes *exactly* only in the limit $M \rightarrow \infty$, thus Equation (A30) becomes equivalent to the time-dependent Schrödinger equation. On the other side, the MCTDH-X method with one orbital, i.e., $M = 1$, is equivalent to the Gross–Pitaevskii mean-field where only one coefficient $C_{0,0,\dots,N,\dots,0}(t)$ contributes. Therefore, the accuracy of MCTDH-X strongly depends on the choice of the number of orbitals M used in the simulations and the convergence of the MCTDH-X results can be improved by increasing the number of orbitals M [27,28,82,85].

We have used the freely available software implementation MCTDHB [14] within the MCTDH-X package [52,86] where the spatial discretization relies on a discrete variable representation (DVR) combined with a fast Fourier transformation [87]. In practice, we have used $M \in \{8, 20\}$ orbitals, $x_{\max} = -x_{\min} = 12$ and $N_x = 512$ grid points. With these parameters employed in MCTDH-X, the absolute error of the eigenenergies—computed by improved relaxation—for two interacting particles in a harmonic trap, with respect to the exact ones, is found to be at the order of 10^{-4} – 10^{-2} . See Refs. [27,28,82,85] for more details about the convergence of the method.

References

1. Serwane, F.; Zürn, G.; Lompe, T.; Ottenstein, T.; Wenz, A.; Jochim, S. Deterministic preparation of a tunable few-fermion system. *Science* **2011**, *332*, 336–338. [[CrossRef](#)]
2. Murmann, S.; Bergschneider, A.; Klinkhamer, V.M.; Zürn, G.; Lompe, T.; Jochim, S. Two Fermions in a Double Well: Exploring a Fundamental Building Block of the Hubbard Model. *Phys. Rev. Lett.* **2015**, *114*, 080402. [[CrossRef](#)]
3. Morsch, O.; Oberthaler, M. Dynamics of Bose-Einstein condensates in optical lattices. *Rev. Mod. Phys.* **2006**, *78*, 179. [[CrossRef](#)]
4. Albiez, M.; Gati, R.; Fölling, J.; Hunsmann, S.; Cristiani, M.; Oberthaler, M.K. Direct observation of tunneling and nonlinear self-trapping in a single bosonic Josephson junction. *Phys. Rev. Lett.* **2005**, *95*, 010402. [[CrossRef](#)] [[PubMed](#)]
5. Jördens, R.; Strohmaier, N.; Günter, K.; Moritz, H.; Esslinger, T. A Mott insulator of fermionic atoms in an optical lattice. *Nature* **2008**, *455*, 204. [[CrossRef](#)] [[PubMed](#)]
6. Greiner, M.; Mandel, O.; Esslinger, T.; Hänsch, T.W.; Bloch, I. Quantum phase transition from a superfluid to a Mott insulator in a gas of ultracold atoms. *Nature* **2002**, *415*, 39. [[CrossRef](#)] [[PubMed](#)]
7. Bloch, I.; Greiner, M. Exploring quantum matter with ultracold atoms in optical lattices. *Adv. At. Mol. Opt. Phys.* **2005**, *52*, 1–47.
8. Bloch, I.; Dalibard, J.; Zwerger, W. Many-body Physics with ultracold gases. *Rev. Mod. Phys.* **2008**, *80*, 885. [[CrossRef](#)]
9. Bloch, I. Quantum coherence and entanglement with ultracold atoms in optical lattices. *Nature* **2008**, *453*, 1016. [[CrossRef](#)]
10. Gross, C.; Bloch, I. Quantum simulations with ultracold atoms in optical lattices. *Science* **2017**, *357*, 995–1001. [[CrossRef](#)]
11. Schollwöck, U. The density-matrix renormalization group. *Rev. Mod. Phys.* **2005**, *77*, 259. [[CrossRef](#)]
12. Schollwöck, U. The density-matrix renormalization group in the age of matrix product states. *Ann. Phys.* **2011**, *326*, 96–192. [[CrossRef](#)]
13. Wall, M.L.; Carr, L.D. Out-of-equilibrium dynamics with matrix product states. *New J. Phys.* **2012**, *14*, 125015. [[CrossRef](#)]
14. Alon, O.E.; Streltsov, A.I.; Cederbaum, L.S. Multiconfigurational time-dependent Hartree method for bosons: Many-body dynamics of bosonic systems. *Phys. Rev. A* **2008**, *77*, 033613. [[CrossRef](#)]
15. Lode, A.U.J.; Lévêque, C.; Madsen, L.B.; Streltsov, A.I.; Alon, O.E. Colloquium: Multiconfigurational time-dependent Hartree approaches for indistinguishable particles. *Rev. Mod. Phys.* **2020**, *92*, 011001. doi:10.1103/RevModPhys.92.011001. [[CrossRef](#)]
16. Parker, J.; Doherty, B.; Meharg, K.; Taylor, K. Time delay between singly and doubly ionizing wavepackets in laser-driven helium. *J. Phys. B At. Mol. Opt. Phys.* **2003**, *36*, L393. [[CrossRef](#)]
17. Buchleitner, A.; Kolovsky, A. Interaction-induced decoherence of atomic Bloch oscillations. *Phys. Rev. Lett.* **2003**, *91*, 253002. [[CrossRef](#)]
18. Pasek, M.; Orso, G.; Delande, D. Anderson localization of ultracold atoms: Where is the mobility edge? *Phys. Rev. Lett.* **2017**, *118*, 170403. [[CrossRef](#)]
19. Davies, E.B. *Quantum Theory of Open Systems*; Academic Press: Cambridge, MA, USA, 1976.
20. Alicki, R.; Lendi, K. *Quantum Dynamical Semigroups and Applications*; Springer: Berlin/Heidelberg, Germany, 2007.
21. Gardiner, C.; Zoller, P. *Quantum Noise: A Handbook of Markovian and non-Markovian Quantum Stochastic Methods with Applications to Quantum Optics*, 3rd ed.; Springer: Berlin/Heidelberg, Germany, 2004.

22. Breuer, H.P.; Petruccione, F. *The Theory of Open Quantum Systems*; Oxford University Press: Oxford, UK, 2002.
23. Schlagheck, P.; Ullmo, D.; Urbina, J.D.; Richter, K.; Tomsovic, S. Enhancement of Many-Body Quantum Interference in Chaotic Bosonic Systems: The Role of Symmetry and Dynamics. *Phys. Rev. Lett.* **2019**, *123*, 215302. [[CrossRef](#)]
24. Guhr, T.; Müller-Groeling, A.; Weidenmüller, H.A. Random-matrix theories in quantum physics: Common concepts. *Phys. Rep.* **1998**, *299*, 189–425. [[CrossRef](#)]
25. Walschaers, M.; Kuipers, J.; Buchleitner, A. From many-particle interference to correlation spectroscopy. *Phys. Rev. A* **2016**, *94*, 020104. [[CrossRef](#)]
26. Lindinger, J.; Buchleitner, A.; Rodriguez, A. Many-Body Multifractality throughout Bosonic Superfluid and Mott Insulator Phases. *Phys. Rev. Lett.* **2019**, *122*, 106603. [[CrossRef](#)] [[PubMed](#)]
27. Lode, A.U.J.; Sakmann, K.; Alon, O.E.; Cederbaum, L.S.; Streltsov, A.I. Numerically exact quantum dynamics of bosons with time-dependent interactions of harmonic type. *Phys. Rev. A* **2012**, *86*, 063606. [[CrossRef](#)]
28. Fasshauer, E.; Lode, A.U.J. Multiconfigurational time-dependent Hartree method for fermions: Implementation, exactness, and few-fermion tunneling to open space. *Phys. Rev. A* **2016**, *93*, 033635. [[CrossRef](#)]
29. Walschaers, M.; Schlawin, F.; Wellens, T.; Buchleitner, A. Quantum transport on disordered and noisy networks: An interplay of structural complexity and uncertainty. *Annu. Rev. Condens. Matter Phys.* **2016**, *7*, 223–248. [[CrossRef](#)]
30. Carnio, E.G.; Hine, N.D.; Römer, R.A. Resolution of the exponent puzzle for the Anderson transition in doped semiconductors. *Phys. Rev. B* **2019**, *99*, 081201. [[CrossRef](#)]
31. Fölling, S.; Trotzky, S.; Cheinet, P.; Feld, M.; Saers, R.; Widera, A.; Müller, T.; Bloch, I. Direct observation of second-order atom tunnelling. *Nature* **2007**, *448*, 1029. [[CrossRef](#)]
32. Milburn, G.; Corney, J.; Wright, E.M.; Walls, D. Quantum dynamics of an atomic Bose-Einstein condensate in a double-well potential. *Phys. Rev. A* **1997**, *55*, 4318. [[CrossRef](#)]
33. Smerzi, A.; Fantoni, S.; Giovanazzi, S.; Shenoy, S. Quantum coherent atomic tunneling between two trapped Bose-Einstein condensates. *Phys. Rev. Lett.* **1997**, *79*, 4950. [[CrossRef](#)]
34. Menotti, C.; Anglin, J.; Cirac, J.; Zoller, P. Dynamic splitting of a Bose-Einstein condensate. *Phys. Rev. A* **2001**, *63*, 023601. [[CrossRef](#)]
35. Mahmud, K.W.; Perry, H.; Reinhardt, W.P. Quantum phase-space picture of Bose-Einstein condensates in a double well. *Phys. Rev. A* **2005**, *71*, 023615. [[CrossRef](#)]
36. Salgueiro, A.; de Toledo Piza, A.; Lemos, G.; Drumond, R.; Nemes, M.; Weidemüller, M. Quantum dynamics of bosons in a double-well potential: Josephson oscillations, self-trapping and ultralong tunneling times. *Eur. Phys. J. D* **2007**, *44*, 537–540. [[CrossRef](#)]
37. Murphy, D.; McCann, J.; Goold, J.; Busch, T. Boson pairs in a one-dimensional split trap. *Phys. Rev. A* **2007**, *76*, 053616. [[CrossRef](#)]
38. Murphy, D.; McCann, J. Low-energy excitations of a boson pair in a double-well trap. *Phys. Rev. A* **2008**, *77*, 063413. [[CrossRef](#)]
39. Streltsov, A.I.; Alon, O.E.; Cederbaum, L.S. Role of excited states in the splitting of a trapped interacting Bose-Einstein condensate by a time-dependent barrier. *Phys. Rev. Lett.* **2007**, *99*, 030402. [[CrossRef](#)]
40. Sakmann, K.; Streltsov, A.I.; Alon, O.E.; Cederbaum, L.S. Exact Quantum Dynamics of a Bosonic Josephson Junction. *Phys. Rev. Lett.* **2009**, *103*, 220601. [[CrossRef](#)] [[PubMed](#)]
41. Zöllner, S.; Meyer, H.D.; Schmelcher, P. Ultracold few-boson systems in a double-well trap. *Phys. Rev. A* **2006**, *74*, 053612. [[CrossRef](#)]
42. Zöllner, S.; Meyer, H.D.; Schmelcher, P. Excitations of few-boson systems in one-dimensional harmonic and double wells. *Phys. Rev. A* **2007**, *75*, 043608. [[CrossRef](#)]
43. Zöllner, S.; Meyer, H.D.; Schmelcher, P. Tunneling dynamics of a few bosons in a double well. *Phys. Rev. A* **2008**, *78*, 013621. [[CrossRef](#)]
44. Zöllner, S.; Meyer, H.D.; Schmelcher, P. Few-Boson dynamics in double wells: From single-atom to correlated pair tunneling. *Phys. Rev. Lett.* **2008**, *100*, 040401. [[CrossRef](#)]
45. Theisen, M.; Streltsov, A.I. Many-body excitations and deexcitations in trapped ultracold bosonic clouds. *Phys. Rev. A* **2016**, *94*, 053622. [[CrossRef](#)]
46. Dobrzyniecki, J.; Sowiński, T. Exact dynamics of two ultra-cold bosons confined in a one-dimensional double-well potential. *Eur. Phys. J. D* **2016**, *70*, 83. [[CrossRef](#)]

47. Spagnolli, G.; Semeghini, G.; Masi, L.; Ferioli, G.; Trenkwalder, A.; Coop, S.; Landini, M.; Pezze, L.; Modugno, G.; Inguscio, M.; et al. Crossing over from attractive to repulsive interactions in a tunneling bosonic Josephson junction. *Phys. Rev. Lett.* **2017**, *118*, 230403. [[CrossRef](#)] [[PubMed](#)]
48. Parra-Murillo, C.A.; Madronero, J.; Wimberger, S. Two-band Bose-Hubbard model for many-body resonant tunneling in the Wannier-Stark system. *Phys. Rev. A* **2013**, *88*, 032119. [[CrossRef](#)]
49. Kolovsky, A.R.; Buchleitner, A. Floquet-Bloch operator for the Bose-Hubbard model with static field. *Phys. Rev. E* **2003**, *68*, 056213. [[CrossRef](#)]
50. Kolovsky, A.R.; Buchleitner, A. Quantum chaos in the Bose-Hubbard model. *Europhys. Lett.* **2004**, *68*, 632. [[CrossRef](#)]
51. Lode, A.U.J. Multiconfigurational time-dependent Hartree method for bosons with internal degrees of freedom: Theory and composite fragmentation of multicomponent Bose-Einstein condensates. *Phys. Rev. A* **2016**, *93*, 063601. [[CrossRef](#)]
52. Lode, A.U.J.; Tsatsos, M.C.; Fasshauer, E.; Lin, R.; Papariello, L.; Mognini, P.; Lévêque, C.; Weiner, S.E. MCTDH-X: The Time-Dependent Multiconfigurational Hartree for Indistinguishable Particles Software. 2020. Available online: <http://ultracold.org> (accessed on 24 March 2020).
53. Nguyen, J.; Tsatsos, M.; Luo, D.; Lode, A.U.J.; Telles, G.; Bagnato, V.; Hulet, R. Parametric excitation of a Bose-Einstein condensate: From Faraday waves to granulation. *Phys. Rev. X* **2019**, *9*, 011052. [[CrossRef](#)]
54. Olshani, M. Atomic scattering in the presence of an external confinement and a gas of impenetrable bosons. *Phys. Rev. Lett.* **1998**, *81*, 938. [[CrossRef](#)]
55. Hunn, S.; Zimmermann, K.; Hiller, M.; Buchleitner, A. Tunneling decay of two interacting bosons in an asymmetric double-well potential: A spectral approach. *Phys. Rev. A* **2013**, *87*, 043626. [[CrossRef](#)]
56. Schäfer, F. Dynamics and Spectral Structure of Strongly Interacting Bosons in a Double Well. Master's Thesis, Albert-Ludwigs-Universität Freiburg, Freiburg, Germany, March 2018. [[CrossRef](#)]
57. Mack, H.; Freyberger, M. Dynamics of entanglement between two trapped atoms. *Phys. Rev. A* **2002**, *66*, 042113. [[CrossRef](#)]
58. Sun, B.; Zhou, D.L.; You, L. Entanglement between two interacting atoms in a one-dimensional harmonic trap. *Phys. Rev. A* **2006**, *73*, 012336. [[CrossRef](#)]
59. Sowiński, T.; Brewczyk, M.; Gajda, M.; Rzażewski, K. Dynamics and decoherence of two cold bosons in a one-dimensional harmonic trap. *Phys. Rev. A* **2010**, *82*, 053631. [[CrossRef](#)]
60. Ghirardi, G.; Marinatto, L. Entanglement and properties. *Fortschritte der Physik* **2003**, *51*, 379–387. [[CrossRef](#)]
61. Ghirardi, G.; Marinatto, L. General criterion for the entanglement of two indistinguishable particles. *Phys. Rev. A* **2004**, *70*, 012109. [[CrossRef](#)]
62. Ghirardi, G.; Marinatto, L. Criteria for the entanglement of composite systems with identical particles. *Fortschritte der Physik* **2004**, *52*, 1045–1051. [[CrossRef](#)]
63. Benatti, F.; Floreanini, R.; Marzolino, U. Entanglement and squeezing with identical particles: Ultracold atom quantum metrology. *J. Phys. B* **2011**, *44*, 091001. [[CrossRef](#)]
64. Tichy, M.C.; de Melo, F.; Kuś, M.; Mintert, F.; Buchleitner, A. Entanglement of identical particles and the detection process. *Fortschritte der Physik* **2013**, *61*, 225. [[CrossRef](#)]
65. Hunn, S. Microscopic Theory of Decaying Many-Particle Systems. Ph.D. Thesis, Albert-Ludwigs-Universität Freiburg, Freiburg, Germany, September 2013.
66. Busch, T.; Englert, B.G.; Rzażewski, K.; Wilkens, M. Two cold atoms in a harmonic trap. *Found. Phys.* **1998**, *28*, 549–559. [[CrossRef](#)]
67. Sakmann, K.; Streltsov, A.I.; Alon, O.E.; Cederbaum, L.S. Reduced density matrices and coherence of trapped interacting bosons. *Phys. Rev. A* **2008**, *78*, 023615. [[CrossRef](#)]
68. Sakmann, K.; Streltsov, A.I.; Alon, O.E.; Cederbaum, L.S. Universality of fragmentation in the Schrödinger dynamics of bosonic Josephson junctions. *Phys. Rev. A* **2014**, *89*, 023602. [[CrossRef](#)]
69. Dobrzyniecki, J.; Sowiński, T. Effective two-mode description of a few ultra-cold bosons in a double-well potential. *Phys. Lett. A* **2018**, *382*, 394–399. [[CrossRef](#)]
70. Dobrzyniecki, J.; Li, X.; Nielsen, A.E.; Sowiński, T. Effective three-body interactions for bosons in a double-well confinement. *Phys. Rev. A* **2018**, *97*, 013609. [[CrossRef](#)]
71. Shin, Y.; Saba, M.; Pasquini, T.; Ketterle, W.; Pritchard, D.; Leanhardt, A. Atom interferometry with Bose-Einstein condensates in a double-well potential. *Phys. Rev. Lett.* **2004**, *92*, 050405. [[CrossRef](#)] [[PubMed](#)]

72. Orzel, C.; Tuchman, A.; Fenselau, M.; Yasuda, M.; Kasevich, M. Squeezed states in a Bose-Einstein condensate. *Science* **2001**, *291*, 2386–2389. [[CrossRef](#)]
73. Ebert, M.; Volosniev, A.; Hammer, H.W. Two cold atoms in a time-dependent harmonic trap in one dimension. *Annalen der Physik* **2016**, *528*, 693–704. [[CrossRef](#)]
74. Streltsov, A.I.; Sakmann, K.; Alon, O.E.; Cederbaum, L.S. Accurate multi-boson long-time dynamics in triple-well periodic traps. *Phys. Rev. A* **2011**, *83*, 043604. [[CrossRef](#)]
75. Alon, O.E. Analysis of a Trapped Bose-Einstein Condensate in Terms of Position, Momentum, and Angular-Momentum Variance. *Symmetry* **2019**, *11*, 1344. [[CrossRef](#)]
76. Marston, C.C.; Balint-Kurti, G.G. The Fourier grid Hamiltonian method for bound state eigenvalues and eigenfunctions. *J. Chem. Phys.* **1989**, *91*, 3571–3576. [[CrossRef](#)]
77. Balint-Kurti, G.G.; Ward, C.L.; Marston, C.C. Two computer programs for solving the Schrödinger equation for bound-state eigenvalues and eigenfunctions using the Fourier grid Hamiltonian method. *Comput. Phys. Commun.* **1991**, *67*, 285–292. [[CrossRef](#)]
78. Kahan, W. Pracniques: Further remarks on reducing truncation errors. *Commun. ACM* **1965**, *8*, 40. [[CrossRef](#)]
79. Muth, D.; Fleischhauer, M.; Schmidt, B. Discretized versus continuous models of p-wave interacting fermions in one dimension. *Phys. Rev. A* **2010**, *82*, 013602. [[CrossRef](#)]
80. Polizzi, E.; Kestyn, J. FEAST Eigenvalue Solver v3. 0 User Guide. *arXiv* **2012**, arXiv:1203.4031.
81. Polizzi, E. Density-matrix-based algorithm for solving eigenvalue problems. *Phys. Rev. B* **2009**, *79*, 115112. [[CrossRef](#)]
82. Lode, A.U.J.; Bruder, C. Dynamics of Hubbard Hamiltonians with the multiconfigurational time-dependent Hartree method for indistinguishable particles. *Phys. Rev. A* **2016**, *94*, 013616. [[CrossRef](#)]
83. Wells, T.; Lode, A.U.J.; Bagnato, V.S.; Tsatsos, M. Vortex reconnections in anisotropic trapped three-dimensional Bose-Einstein condensates. *J. Low Temp. Phys.* **2015**, *180*, 133–143. [[CrossRef](#)]
84. Kramer, P.; Saraceno, M. *Geometry of the Time-Dependent Variational Principle in Quantum Mechanics*; Springer: Berlin/Heidelberg, Germany, 1981.
85. Conte, D.; Lubich, C. An error analysis of the multi-configuration time-dependent Hartree method of quantum dynamics. *ESAIM Math. Model. Numer. Anal.* **2010**, *44*, 759–780. [[CrossRef](#)]
86. Lin, R.; Mognini, P.; Papariello, L.; Tsatsos, M.C.; Leveque, C.; Weiner, S.E.; Fasshauer, E.; Chitra, R.; Lode, A.U.J. MCTDH-X: The multiconfigurational time-dependent Hartree method for indistinguishable particles software. *Quantum Sci. Technol.* **2020**. [[CrossRef](#)]
87. Beck, M.H.; Jäckle, A.; Worth, G.A.; Meyer, H.D. The multiconfiguration time-dependent Hartree (MCTDH) method: A highly efficient algorithm for propagating wavepackets. *Phys. Rep.* **2000**, *324*, 1–105. [[CrossRef](#)]



© 2020 by the authors. Licensee MDPI, Basel, Switzerland. This article is an open access article distributed under the terms and conditions of the Creative Commons Attribution (CC BY) license (<http://creativecommons.org/licenses/by/4.0/>).